Constrained Control of Low-Capacitance Delta Cascaded H-Bridge StatComs: A Model Predictive Control Approach

Ezequiel Rodriguez, *Student Member, IEEE,* Ramon Leyva, *Senior Member, IEEE*, Christopher D. Townsend, *Member, IEEE,* Glen G. Farivar, *Senior Member, IEEE,* Hossein Dehghani Tafti, *Member, IEEE,* and Josep Pou, *Fellow, IEEE*

***Abstract*—This paper presents a constrained model predictive control (MPC) strategy for a three-phase low-capacitance static compensator (LC-StatCom) with delta configuration. The controller consists of an outer loop that provides dynamic references for the active grid current component and the circulating current; whereas the inner predictive loop minimises the quadratic error of state variables subject to operating limit conditions, thus providing optimal control signals that produce a fast response while guaranteeing the prescribed safe operating limit conditions. The paper also proposes an enhanced discrete-time model, which uses intersample values, that improves the accuracy of the model predictions when the sampling rate is not high enough to assume constant state variables. As a result, it facilitates the implementation of MPC on less powerful processors compared to the conventional modeling. The proposed control is especially suited for the LC-StatComs since it incorporates analytical computation of desired steady-state trajectories, which takes into account the induced oscillation on the capacitor voltages that are inherent to the LC-StatComs. The proposed approach has been verified by simulation and experimentally with a laboratory prototype.**

I. Introduction

The low-capacitance static compensator (LC-StatCom[1]) based on the cascaded H-bridge (CHB) multilevel converter [1]–[7], is an incipient alternative for the next generation of StatCom systems for transmission and distribution grids. The LC-StatCom concept allows reducing the converter size and cost for a given rated power. Nevertheless, the reduced capacitance, and thus low energy stored in the converter, inflicts the LC-StatCom with i) a large magnitude low-frequency voltage oscillation, and ii) a nonnegligible coupling between the capacitor voltage dynamics and the inductor current dynamics. These particularities make the LC-StatCom control challenging.

Some early work on the control design of the LC-StatCom was presented in [1], [2], [8], where the main objective was to increase the control effectiveness by using analytic feedforward filtering techniques to substitute the conventional low-pass filter that reduces the response bandwidth. The design and control of an LC-StatCom were also discussed in [9], [10], where a second-order generalised integrator (SOGI) was used to estimate the maximum capacitor voltage. Thus effectively obtaining a fast estimation of the variable to regulate. A multi-input linear time-variant control law, based on incremental passivity theory, that ensures large-signal stability was used to control the LC-StatCom in [11]. This method achieved a fast dynamic but as for the rest of the aforementioned references, the focus was to address the control problems within a phase and hence, a single-phase LC-StatCom was used for demonstration.

With regard to the three-phase LC-StatComs, references [7], [12], [13] are worthwhile highlighting, where the use of third-harmonic zero-sequence to achieve improved performance of the LC-StatComs is discussed. Particularly, [7], [13] cover in detail the restricted region of operation in inductive mode. However, achieving fast response and constraining the state variables during transients was overlooked.

Compared to the LC-StatCom, the control of conventional StatComs is a much more comprehensively studied field [14]–[18]. In this regard, cascade approach is one of the established popular control options. The inner current control loop can be based on voltage oriented control (VOC) [19], [20], as in the previous references, or using proportional plus resonant current controllers, as in [9]. The outer control loop regulates and balances the capacitor voltages by modifying the references used in the inner current control loop. This represents a common approach to compensate converter parametric uncertainties. However, none of these control schemes enforces a limitation on the capacitor voltages during the transient operation.

In the LC-StatComs, due to the large induced capacitor voltage oscillations, it is important to limit the capacitor voltages within a predefined range. Thus, there is a need for a three-phase LC-StatCom control strategy that considers the particularities of the LC-StatCom and delivers a fast dynamic while confining the sate variables, i.e. the capacitor voltages and the inductor currents, in safe operating regions.

Model predictive control (MPC) is an attractive way to deal with operating limit conditions [21], [22]. Several authors have studied the MPC application for StatCom control [23]–[26]. In [23], a partially stratified MPC approach (current and capacitor voltage control solved sequentially) is applied to a StatCom with star configuration. In [24] and [25], the MPC formulation concerns with modulation-related problems, resulting in high-quality voltages at relatively low switching

[1]Note that the LC acronym in LC-StatCom refers to low-capacitance and not to the widely used LC filter.

frequencies. A heuristic MPC approach is analysed in [24] for a StatCom with star configuration, whereas an optimal pulse pattern MPC technique is analysed in [25] for a StatCom with delta configuration. A fault detection and localization algorithm based on MPC is proposed in [26] for a single-phase CHB. All the aforementioned MPC references consider a conventional StatCom. Adapting these techniques to the particularities of LC-StatComs is a contribution of this paper. This paper describes the design of a constrained control approach, based on the MPC, for the LC-StatComs. Adapting the MPC to the LC-StatCom requires taking into account new considerations:

1) Design of an outer control loop that properly handles converter parametric uncertainty by using the time-varying capacitor energies.
2) Due to the reduced capacitor size in the LC-StatComs, the bilinear terms of their dynamics should be taken into account.
3) Modelling and inclusion of the capacitor voltage constraints in the underlying optimisation problem, so that safe operating conditions are guaranteed during transients.
4) Due to the reduced capacitor size, the low-frequency voltage oscillation on the capacitors is not negligible and, therefore, must be taken into account when designing the system references (state variables and control signals at equilibrium trajectory).
5) Choosing an optimisation algorithm that minimises computational burden and facilitates real-time digital control.

Addressing the above considerations, the paper proposes a scheme based on the common cascade loop structure [15], where voltage and current magnitudes are constrained using an MPC approach. In the MPC approach, the calculation of the prediction errors takes into account the desired state trajectory in transient and steady-state operation. In steady-state operation, trajectories are calculated according to the converter model, as in [11]. Transients in the desired state trajectory consider uncertainty according to [14], whereas the calculation of the prediction errors takes into account the bilinear nature of the converter. Also, an optimisation algorithm with low iteration cost based on the alternating direction method of multipliers (ADMM) has been chosen to do the experimental implementation.

The paper is organised as follows. Section II describes the modelling of the LC-StatCom with delta configuration, where the discrete-time model is derived. The section also reviews the common Euler approximation model and proposes a new one that does not neglect the bilinear terms. Based on the model, the proposed constrained MPC is described in detail in Section III, in which the state trajectory, constraints modelling, and the resultant optimisation problem are specifically addressed. Section IV provides experimental results to corroborate the performance of the proposed approach. In addition, complementary simulation results, which show multilevel waveforms, are presented in Section V. Section VI summarises the conclusions of the paper.

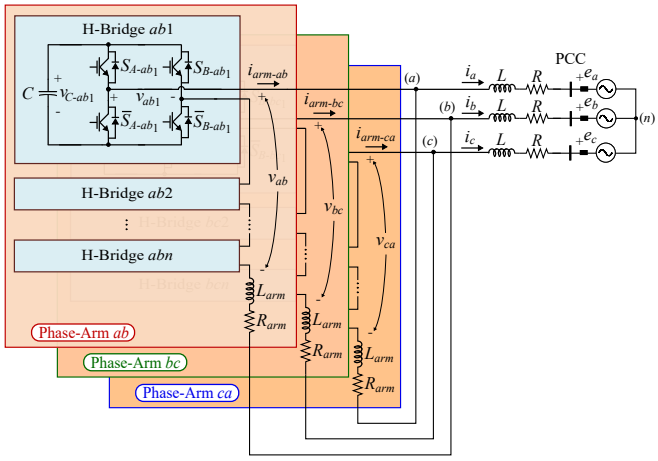

Fig. 1. Circuit diagram of the LC-StatCom with delta configuration.

II. LC-StatCom with Delta Configuration

This section reviews the topology of the LC-StatCom with delta configuration, its state variables, and its state-space model. Then, the averaged model of the system is derived, and subsequently discretised. The discretised model is used in the proposed constrained MPC, which is explained in the next section.

A. Topology

The converter topology is shown in Fig. 1. The power converter consists of three identical phase-arms $x \in \mathcal{X} = \{ab,\, bc,\, ca\}$ with delta configuration. Each phase-arm includes n series-connected H-bridges $j \in \mathcal{J} = \{1, 2, \ldots, n\}$, and an arm inductor L_{arm}. Each H-bridge consists of a floating capacitor C at its dc-side, and two pairs of power switches that work in a complementary manner, which allows the generation of three different output voltage levels. The three ac terminals of the power converter (a), (b), (c) are connected to the point of common coupling (PCC) grid voltages e_a, e_b, e_c through the filtering inductors L. Losses are also modeled with the series resistances R and R_{arm}, as depicted in Fig. 1.

B. CHB Multilevel Converter Modelling

In the CHB multilevel converter with n series-connected H-bridges per phase-arm, shown in Fig. 1, each converter voltage v_x is the sum of the individual H-bridge ac voltages, i.e., $v_x = \sum_{j\in\mathcal{J}} v_{xj}$. The ac- and dc-sides of the converter, in the j^{th} H-bridge for the x^{th} phase-arm, are related by the discontinuous control function S_{xj} as:

$$\begin{aligned} v_{xj} &= S_{xj} v_{C-xj}, \\ C\tfrac{d}{dt} v_{C-xj} &= -S_{xj} i_{arm-x}, \end{aligned} \tag{1}$$

where v_{C-xj} is the capacitor voltage. Note that it has been considered that all the H-bridges have the same nominal capacitance value C.

The discrete term $S_{xj} = S_{A-xj} - S_{B-xj}$ belongs to the finite set $\{-1,\, 0,\, 1\}$, where $S_{A-xj},\, S_{B-xj} \in \{0,\, 1\}$ correspond to the switching states of the top switches (according to Fig. 1).

The phase-arm converter voltages v_{ab}, v_{bc}, v_{ca} can be related with their corresponding cluster voltages (sum-capacitor-voltages), i.e., $v_{\Sigma-ab} = \sum_{j\in\mathcal{J}} v_{C-abj}$ for the phase-arm ab, and similarly for arms bc and ca, as

$$v_x = S_x v_{\Sigma-x}, \tag{2}$$

where the equivalent switching function S_x corresponds to

$$S_x = \frac{1}{n}\sum_{j\in\mathcal{J}} S_{xj} \in \left\{-1,\ \frac{-n+1}{n},\ \ldots\ 0\ \ldots,\ \frac{n-1}{n},\ 1\right\}. \tag{3}$$

Note that this assumes that the capacitor voltages are balanced within the converter phase-arm ($v_{C-xj} = v_{\Sigma-x}/n,\ \forall j,\ x$). This implies that an interbridge balancing algorithm is implemented within the control in order to fulfill this assumption [27].

Similarly, the arm currents i_{arm-ab}, i_{arm-bc}, i_{arm-ca} can be related with their corresponding cluster voltage variations, as

$$\frac{C}{n}\frac{d}{dt} v_{\Sigma-x} = -S_x i_{arm-x}, \tag{4}$$

which governs the cluster voltage dynamics.

Inductor current dynamics are determined by applying Kirchhoff's voltage law in the circuit shown in Fig. 1. The details to derive the differential equations that define the current dynamics are provided in the Appendix.

C. Bilinear Continuous-Time Averaged Model

The number of levels of the equivalent switching functions S_{ab}, S_{bc}, S_{ca}, which can be generated due to the switching nature of the converter, is finite, as (3) indicates. The equivalent switching functions in (3) can be approximated by their averaged values over a switching period, thus the modulation signals δ_{ab}, δ_{bc}, δ_{ca} correspond to

$$\delta_x = \frac{1}{T_{sw}}\int_{t-T_{sw}}^{t} S_x dt \in [-1,\ 1]. \tag{5}$$

The switching period T_{sw} is assumed much (at least 10 times) shorter than the converter system time constants.

Then, the ac- and dc-sides of the converter in the averaged model are related by the continuous modulation function δ_x. The variables of the model are considered henceforth to be averaged variables. For the purpose of simplicity, no difference in notation between the averaged and exact variables has been included.

The dynamic behaviour of the CHB converter uses as state variables the grid currents i_a and i_b, together with the circulating current i_{circ}, and the cluster voltages $v_{\Sigma-ab}$, $v_{\Sigma-bc}$, $v_{\Sigma-ca}$; and the control inputs in the model correspond to the modulation signals δ_{ab}, δ_{bc}, δ_{ca}. The state variables are grouped in the vector $\boldsymbol{x} \in \mathbb{R}^6$, the control inputs are grouped in the vector $\boldsymbol{u} \in \mathbb{R}^3$, and the PCC grid voltages are grouped in the vector $\boldsymbol{e} \in \mathbb{R}^3$, as:

$$\begin{aligned} \boldsymbol{x} &= \left[i_a\ i_b\ i_{circ}\ v_{\Sigma-ab}\ v_{\Sigma-bc}\ v_{\Sigma-ca}\right]^T, \\ \boldsymbol{u} &= \left[\delta_{ab}\ \delta_{bc}\ \delta_{ca}\right]^T, \\ \boldsymbol{e} &= \left[e_a\ e_b\ e_c\right]^T. \end{aligned} \tag{6}$$

Using (85) and (4), the following nonlinear state-space model with continuous variables is obtained

$$\dot{\boldsymbol{x}} = \boldsymbol{A}\boldsymbol{x} + \boldsymbol{B}(\boldsymbol{x})\,\boldsymbol{u} + \boldsymbol{W}\boldsymbol{e}, \tag{7}$$

where the system matrix $\boldsymbol{A}$, input matrix $\boldsymbol{B}(\boldsymbol{x})$, and matrix $\boldsymbol{W}$, correspond to:

$$\boldsymbol{A} = \begin{bmatrix} \boldsymbol{A}_{11} & \boldsymbol{0}_{3\times3} \\ \boldsymbol{0}_{3\times3} & \boldsymbol{0}_{3\times3} \end{bmatrix}, \tag{8}$$

$$\boldsymbol{B}(\boldsymbol{x}) = \begin{bmatrix} \boldsymbol{b}_1(\boldsymbol{x}) & \boldsymbol{b}_2(\boldsymbol{x}) & \boldsymbol{b}_3(\boldsymbol{x}) \end{bmatrix}, \tag{9}$$

$$\boldsymbol{W} = -\frac{1}{3L_{eq}}\begin{bmatrix} 2 & -1 & -1 \\ -1 & 2 & -1 \\ 0 & 0 & 0 \\ 0 & 0 & 0 \\ 0 & 0 & 0 \\ 0 & 0 & 0 \end{bmatrix}, \tag{10}$$

with

$$\boldsymbol{A}_{11} = \begin{bmatrix} -\frac{R_{eq}}{L_{eq}} & 0 & 0 \\ 0 & -\frac{R_{eq}}{L_{eq}} & 0 \\ 0 & 0 & -\frac{R_{arm}}{L_{arm}} \end{bmatrix}, \tag{11}$$

$$\boldsymbol{b}_1(\boldsymbol{x}) = \begin{bmatrix} \frac{1}{3L_{eq}} v_{\Sigma-ab} \\ -\frac{1}{3L_{eq}} v_{\Sigma-ab} \\ \frac{1}{3L_{arm}} v_{\Sigma-ab} \\ -\frac{1}{3C/n}\left(i_a - i_b + 3i_{circ}\right) \\ 0 \\ 0 \end{bmatrix}, \tag{12}$$

$$\boldsymbol{b}_2(\boldsymbol{x}) = \begin{bmatrix} 0 \\ \frac{1}{3L_{eq}} v_{\Sigma-bc} \\ \frac{1}{3L_{arm}} v_{\Sigma-bc} \\ 0 \\ -\frac{1}{3C/n}\left(i_a + 2i_b + 3i_{circ}\right) \\ 0 \end{bmatrix}, \tag{13}$$

$$\boldsymbol{b}_3(\boldsymbol{x}) = \begin{bmatrix} -\frac{1}{3L_{eq}} v_{\Sigma-ca} \\ 0 \\ \frac{1}{3L_{arm}} v_{\Sigma-ca} \\ 0 \\ 0 \\ -\frac{1}{3C/n}\left(-2i_a - i_b + 3i_{circ}\right) \end{bmatrix}. \tag{14}$$

Note that the terms of $\boldsymbol{B}(\boldsymbol{x})$ depend linearly on the state $\boldsymbol{x}$, and $\boldsymbol{B}(\boldsymbol{x})$ is multiplied by the control vector $\boldsymbol{u}$, thus showing a bilinear nature of (7).

D. Discrete-Time Averaged Model

Because of the discrete-time implementation of the MPC controller, a discrete-time representation of the model in (7) is needed.

Assuming that the state $\boldsymbol{x}$, the input $\boldsymbol{u}$, and the voltage $\boldsymbol{e}$, are approximately constant between the sampling instants k and $k+1$, the discrete-time model corresponds to

$$\boldsymbol{x}(k+1) = \boldsymbol{A}_d'\boldsymbol{x}(k) + \boldsymbol{B}_d'(\boldsymbol{x}(k))\,\boldsymbol{u}(k) + \boldsymbol{W}_d'\boldsymbol{e}(k), \tag{15}$$

with matrices

$$\begin{aligned}
&\boldsymbol{A}_d^{'} = e^{\boldsymbol{A}T_s} \\
&\boldsymbol{B}_d^{'}\left(\boldsymbol{x}\left(k\right)\right) = \left(\int_{\tau=0}^{T_s} e^{\boldsymbol{A}\tau} d\tau\right) \boldsymbol{B}\left(\boldsymbol{x}\left(k\right)\right) \\
&\boldsymbol{W}_d^{'} = \left(\int_{\tau=0}^{T_s} e^{\boldsymbol{A}\tau} d\tau\right) \boldsymbol{W},
\end{aligned} \tag{16}$$

which can be simplified, for short enough sampling periods T_s, assuming the Euler's method, i.e., $e^{\boldsymbol{A}T_s} \approx \boldsymbol{I} + \boldsymbol{A}T_s$. Note that in (16), the matrix $\boldsymbol{B}\left(\boldsymbol{x}\right)$ has been removed from the integral sign as it is assumed constant between k and $k+1$. If the sampling period T_s is long enough, the variations of state $\boldsymbol{x}$ along the sampling period could be nonnegligible, and thus is not appropriate to consider $\boldsymbol{B}\left(\boldsymbol{x}\right)$ with a constant value of $\boldsymbol{x}$ equal to the value sampled at the beginning of the period $\boldsymbol{x}\left(k\right)$. Therefore, the model (15)-(16) demands high sampling rates. As an alternative to using high sampling rates, enhanced dynamic models could accurately predict state variables for longer sampling periods.

Not assuming that the state $\boldsymbol{x}$ and the voltage $\boldsymbol{e}$ are constant between the sampling instants k and $k+1$, implies that the terms $\boldsymbol{B}\left(\boldsymbol{x}\right)$ and $\boldsymbol{W}\boldsymbol{e}$ in (7) vary between the instants k and $k+1$ [28], thus resulting in a more accurate model (17), involving the calculation of integrals $\int_{\tau=0}^{T_s} e^{\boldsymbol{A}\tau}\boldsymbol{B}\left(\boldsymbol{x}\left(\tau\right)\right) d\tau$ and $\int_{\tau=0}^{T_s} e^{\boldsymbol{A}\tau}\boldsymbol{W}\boldsymbol{e}\left(\tau\right) d\tau$,

$$\boldsymbol{x}\left(k+1\right) = \boldsymbol{A}_d\boldsymbol{x}\left(k\right) + \boldsymbol{B}_d\left(\boldsymbol{x}\left(k\right)\right)\boldsymbol{u}\left(k\right) + \boldsymbol{w}_d\left(k\right), \tag{17}$$

with

$$\begin{aligned}
&\boldsymbol{A}_d = e^{\boldsymbol{A}T_s} \\
&\boldsymbol{B}_d\left(\boldsymbol{x}\left(k\right)\right) = \int_{\tau=0}^{T_s} e^{\boldsymbol{A}\tau}\boldsymbol{B}\left(\boldsymbol{x}\left(\tau\right)\right) d\tau \\
&\boldsymbol{w}_d\left(k\right) = \int_{\tau=0}^{T_s} e^{\boldsymbol{A}\tau}\boldsymbol{W}\boldsymbol{e}\left(\tau\right) d\tau.
\end{aligned} \tag{18}$$

The aforementioned integrals can be evaluated in M equal subintervals, which considers the evolution of the state $\boldsymbol{x}$ and the voltage $\boldsymbol{e}$ inside the sampling period T_s. Therefore, (17) and (18) can be simplified by the following accurate discrete-time model that uses intersample values,

$$\boldsymbol{x}\left(k+1\right) = \boldsymbol{A}_d\boldsymbol{x}\left(k\right) + \boldsymbol{B}_d\left(\boldsymbol{x}\left(k\right)\right)\boldsymbol{u}\left(k\right) + \boldsymbol{W}_d\boldsymbol{e}\left(k\right), \tag{19}$$

with

$$\begin{aligned}
&\boldsymbol{A}_d = \left(\boldsymbol{I} + \tfrac{T_s}{M}\boldsymbol{A}\right)^M \\
&\boldsymbol{B}_d\left(\boldsymbol{x}\left(k\right)\right) = \\
&\tfrac{T_s}{M}\textstyle\sum_{m=0}^{M-1}\left(\boldsymbol{I} + \tfrac{T_s}{M}\boldsymbol{A}\right)^{M-1-m}\boldsymbol{B}\left(\boldsymbol{x}\left(k + m\tfrac{T_s}{M}\right)\right) \\
&\boldsymbol{W}_d = \tfrac{T_s}{M}\textstyle\sum_{m=0}^{M-1}\left(\boldsymbol{I} + \tfrac{T_s}{M}\boldsymbol{A}\right)^{M-1-m}\boldsymbol{W}\boldsymbol{R}_\omega^m,
\end{aligned} \tag{20}$$

where $\boldsymbol{x}\left(k + m\frac{T_s}{M}\right)$ is the value of the state inside the sampling period T_s, and the matrix $\boldsymbol{R}_\omega$ represents a rotation during a time T_s/M, i.e.,

$$\boldsymbol{R}_\omega = \boldsymbol{T}_{\alpha\beta}^{\dagger}\begin{bmatrix} \cos\left(\omega\frac{T_s}{M}\right) & -\sin\left(\omega\frac{T_s}{M}\right) \\ \sin\left(\omega\frac{T_s}{M}\right) & \cos\left(\omega\frac{T_s}{M}\right) \end{bmatrix}\boldsymbol{T}_{\alpha\beta}. \tag{21}$$

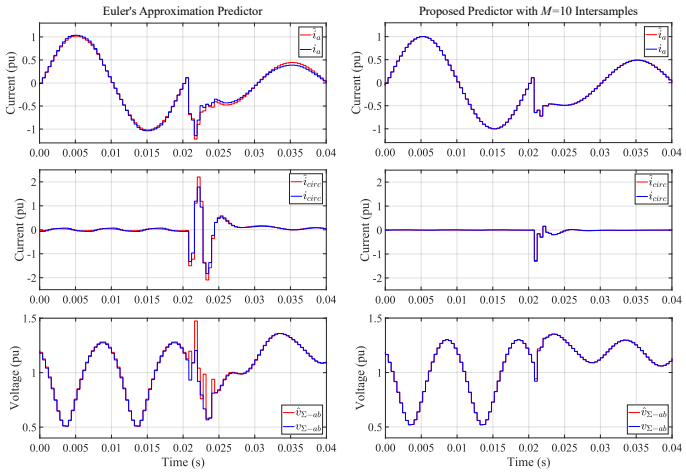

Fig. 2. Simulation waveforms for the proposed controller during a sudden reactive power change from full capacitive to half inductive operation at $t = 0.04$ s. Left plots: Predicted waveforms when using the common predictor (15)-(16); Right plots: Predicted waveforms when using the proposed predictor (19)-(20) with $M = 10$ intersamples. Top plots: Sampled injected current in phase a (blue) and its prediction (red); Middle plots: Sampled circulating current (blue) and its prediction (red); Bottom plot: Sampled cluster voltage in phase-arm ab (blue) and its prediction (red).

Note that matrices $\boldsymbol{T}_{\alpha\beta}$ and $\boldsymbol{T}_{\alpha\beta}^{\dagger}$ correspond to the reduced power conservative Clarke transformation and its pseudoinverse (inverse matrix), respectively, i.e.

$$\begin{aligned}
&\boldsymbol{T}_{\alpha\beta} = \sqrt{\tfrac{2}{3}}\begin{bmatrix} 1 & -\frac{1}{2} & -\frac{1}{2} \\ 0 & \frac{\sqrt{3}}{2} & -\frac{\sqrt{3}}{2} \end{bmatrix}, \quad \text{and} \\
&\boldsymbol{T}_{\alpha\beta}^{\dagger} = \sqrt{\tfrac{2}{3}}\begin{bmatrix} 1 & 0 \\ -\frac{1}{2} & \frac{\sqrt{3}}{2} \\ -\frac{1}{2} & -\frac{\sqrt{3}}{2} \end{bmatrix}.
\end{aligned} \tag{22}$$

Having a good prediction of the state at each instant when the MPC actuates is very important, and this depends on the value of M.

Next, as an illustration, it is shown how the state predictions improve when the proposed intersample model (19)-(20) is used. Particularly, in Fig. 2, the accuracy of the proposed predictor (19)-(20) with $M = 10$ intersamples (right plots) is evaluated and compared with the common approach in (15)-(16) (left plots), when a sudden change in the instantaneous reactive power reference occurs.

Fig. 2 corroborates, when the sampling frequency is 2500 Hz, that both in steady-state and transient operation, the prediction errors are significantly smaller when the bilinear terms are treated as the proposed approach does. As seen in Fig. 2, the proposed predictor is capable of performing very accurately even when the sampling period is relatively large. In comparison, the commonly used predictor method is less accurate, especially during transient operation, deteriorating the overall performance of the controller. In Fig. 2, it can also be observed that the circulating current in steady-state exhibits worse behaviour (low-frequency distortion) when bilinear terms are disregarded, which could affect the system losses. Specifically, an oscillation in the circulating current with approximately 10% magnitude can be observed when

using a common predictor. Furthermore, the harmonic content of the signals improves when bilinear terms are considered. Specifically, the total harmonic distortion (THD) of the StatCom currents improves from 1.46% to 0.30% at full capacitive power. One more observation from Fig. 2 is the large prediction errors in the capacitor voltages during transients when bilinear terms are not considered.

III. Constrained Model Predictive Control

This section presents a constrained control based on MPC for LC-StatComs that tracks the instantaneous real p and imaginary q power references, the instantaneous circulating current i_{circ} references, and the cluster voltage $v_{\Sigma-x}$ references, while limiting the capacitor voltages and the arm currents during transients.

First, the control problem and the proposed hierarchical controller structure are described. Then, system objectives are mapped into cost functions and constraints, which combined define the optimisation problem. Finally, using the proposed predictor (19)-(20), the optimisation problem is formulated as a quadratic programming (QP) problem that can be solved using common methods such as interior-point methods, active-set methods, or alternating direction method of multipliers (ADMM). The interior-point methods have a per iteration cost generally much higher than the ADMM methods [29]. For this reason, an algorithm based on the ADMM has been chosen to do the experimental implementation.

A. Control Problem of the LC-StatCom

The LC-StatCom control is a challenging problem due to i) the large magnitude low-frequency voltage oscillation on the LC-StatCom capacitors, and ii) the nonnegligible coupling between the capacitor voltage dynamics and the inductor current dynamics. Therefore, the control of LC-StatComs has to deal with their bilinear multi-input nature, and has to satisfy a large number of control objectives simultaneously, among them:

- Regulation of the instantaneous powers/currents along their references;
- High bandwidth control of the capacitor voltages;
- Capacitor voltage balancing (interphase and interbridge balancing);
- Maintaining the capacitor voltages and the arm currents within desired limits during transients.

The rest of this section discusses the proposed control to address this challenging problem in the LC-StatComs.

B. Controller Structure

Fig. 3 depicts the hierarchical control block diagram of the proposed constrained MPC applied to a multilevel LC-StatCom. Next, the main blocks are explained.

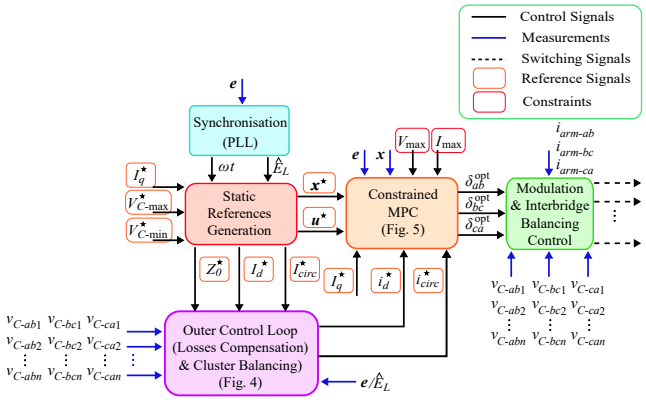

Fig. 3. Block diagram of the proposed constrained MPC using direct-power and outer loops.

1) Constrained MPC: The main block of the control scheme is the "Constrained MPC" block. It computes in real time (in between samples) the optimal modulation functions for each converter phase-arm $\boldsymbol{u}^{\text{opt}} = \begin{bmatrix} \delta_{ab}^{\text{opt}} & \delta_{bc}^{\text{opt}} & \delta_{ca}^{\text{opt}} \end{bmatrix}^T$ that minimise a quadratic cost function J subject to state and input constraints, and the discrete evolution of the bilinear state-space model (19). The optimisation process is repeated every sampling period T_s according to the receding horizon policy. This leads to the following optimisation problem

$$\begin{aligned} \boldsymbol{u}^{\text{opt}}(k) = \arg \underset{\boldsymbol{u}(k)}{\text{minimise}} \quad & J \\ \text{subject to} \quad & \hat{\boldsymbol{x}}(k+1) = \\ & \boldsymbol{A}_d \boldsymbol{x}(k) + \boldsymbol{B}_d(\boldsymbol{x}(k))\,\boldsymbol{u}(k) + \boldsymbol{W}_d \boldsymbol{e}(k) \\ & \hat{\boldsymbol{x}}(k+1) \in \mathbb{X} \\ & \boldsymbol{u}(k) \in \mathbb{U} \end{aligned} \tag{23}$$

where $\mathbb{X}$ and $\mathbb{U}$ represent the admissible domains, while $\hat{\boldsymbol{x}}(k+1)$ denotes the prediction of state $\boldsymbol{x}$ at instant $k+1$.

The optimal modulation functions $\delta_{ab}^{\text{opt}}, \delta_{bc}^{\text{opt}}, \delta_{ca}^{\text{opt}}$ constitute the inputs of block "Modulation & Interbridge Balancing Control", which generates the switching signals for the power converter.

The "Constrained MPC" block uses as input the actual state $\boldsymbol{x}(k)$ and voltage $\boldsymbol{e}(k)$, static references for the state $\boldsymbol{x}^\star(k)$ and the control $\boldsymbol{u}^\star(k)$, dynamic references for the active grid current component $i_d^\star$ and the circulating current $i_{circ}^\star$, and state constraints for the capacitor voltages $V_{\max}$ and the arm currents $I_{\max}$. Static references assume steady-state operation and a set of nominal converter parameters, and they are calculated in block "Static References Generation", according to (7). Dynamic references aim to shape the static references $\boldsymbol{x}^\star(k)$ in order to provide a set of correct references that properly regulate and balance the capacitor voltages despite converter parametric uncertainties. Dynamic references are calculated in the block "Outer Control Loop (Losses Compensation & Cluster Balancing)".

2) Static References Generation: The converter is synchronised with the PCC voltages by using a phase-locked loop (PLL) to calculate the angle ωt and the amplitude $\hat{E}_L$.

Subsequently, based on the knowledge of the PCC voltages, grid reactive power requirement, $I_q^\star$, and the capacitor voltage maximum and minimum, $V_{C-\max}^\star$ and $V_{C-\min}^\star$, coherent reference signals for the rest of the variables are calculated. The coherent reference signals agree with the aforementioned averaged model in (7), hence,

$$\frac{d\boldsymbol{x}^\star}{dt} = \boldsymbol{A}\boldsymbol{x}^\star + \boldsymbol{B}\left(\boldsymbol{x}^\star\right)\boldsymbol{u}^\star + \boldsymbol{W}\boldsymbol{e}, \tag{24}$$

where $\boldsymbol{x}^\star = \begin{bmatrix} i_a^\star & i_b^\star & i_{circ}^\star & v_{\Sigma-ab}^\star & v_{\Sigma-bc}^\star & v_{\Sigma-ca}^\star \end{bmatrix}^T$ represents the desired state trajectory, and $\boldsymbol{u}^\star$ is the applied controller action so that the system remains at the desired trajectory $\boldsymbol{x}^\star$.

The reference values according to (24) are calculated assuming that the PCC voltages and the desired injected StatCom currents correspond to:

$$\begin{aligned} \begin{bmatrix} e_{ab} \\ e_{bc} \\ e_{ca} \end{bmatrix} &= \hat{E}_L \begin{bmatrix} \cos\left(\omega t + \pi/6\right) \\ \cos\left(\omega t - \pi/2\right) \\ \cos\left(\omega t + 5\pi/6\right) \end{bmatrix}, \\ \begin{bmatrix} i_a^\star \\ i_b^\star \\ i_c^\star \end{bmatrix} &= \hat{I}^\star \begin{bmatrix} \cos\left(\omega t + \varphi^\star\right) \\ \cos\left(\omega t + \varphi^\star - 2\pi/3\right) \\ \cos\left(\omega t + \varphi^\star + 2\pi/3\right) \end{bmatrix}. \end{aligned} \tag{25}$$

Parameters $\hat{E}_L$ and $\hat{I}^\star$ represent the amplitudes of the line-to-line PCC voltages and the injected StatCom current references, respectively. The angle $\varphi^\star$ represents the phase difference between the injected currents and the line-to-neutral PCC voltages. Ideally, that is, without losses, $\varphi^\star$ is $\pi/2$ rad in inductive mode and $-\pi/2$ rad in capacitive mode, according to the direction of the currents indicated in Fig. 1.

The amplitude $\hat{I}^\star$ and angle $\varphi^\star$ of the desired injected StatCom currents in (25) can be calculated using their dq components. The q-component ($I_q^\star$) is a known grid requirement, and the d-component ($I_d^\star$) corresponds to

$$I_d^\star = -\frac{2\sqrt{2}\left(R_{eq}I_q^{\star 2} + P_0^\star\right)}{\hat{E}_L\left(1 + \sqrt{1 - 8R_{eq}\left(R_{eq}I_q^{\star 2} + P_0^\star\right)/\hat{E}_L^2}\right)}, \tag{26}$$

where the power conservative $dq0$ transformation has been considered [11]. The power static reference $P_0^\star = 3R_{arm}\left(\hat{I}_{circ}^\star/\sqrt{2}\right)^2$ corresponds to the increment of power in the converter when a static sinusoidal reference of circulating current $I_{circ}^\star$, with amplitude $\hat{I}_{circ}^\star$, is applied during steady-state [15].

Substituting (25) into (84), the arm current references $i_{arm-x}^\star$ can be calculated. Similarly, using (85), the converter voltage references $v_x^\star$ are derived. Once the arm current and converter voltage references are known, the cluster voltage references $v_{\Sigma-x}^\star$ can be calculated by solving the differential equation in (4), i.e.,

$$v_{\Sigma-x}^\star(t) = \sqrt{\left(v_{\Sigma-x}^\star(0)\right)^2 - \frac{2}{C/n}\int_0^t v_x^\star i_{arm-x}^\star dt}, \tag{27}$$

for $x \in \{ab, bc, ca\}$, and where $v_{\Sigma-x}^\star(0)$ is the initial condition. Note that the integrator operator in (27) can be solved analytically, according to (25), (84), and (85). It is important to highlight this reference design criteria stands in contrast with the commonly adopted approach in the conventional StatCom applications, where the capacitor voltages are regarded as constant due to the large capacitance used.

Using the following variable change

$$z_{\Sigma-x}^\star = \frac{1}{2n}\left(v_{\Sigma-x}^\star\right)^2, \tag{28}$$

which is proportional to the capacitive energy stored in a converter phase, and solving (27) for (25) and $I_{circ}^\star = 0$, yields

$$\begin{bmatrix} z_{\Sigma-ab}^\star \\ z_{\Sigma-bc}^\star \\ z_{\Sigma-ca}^\star \end{bmatrix} = \begin{bmatrix} Z_0^\star \\ Z_0^\star \\ Z_0^\star \end{bmatrix} \mp \frac{S^\star}{6\omega_g C} \begin{bmatrix} \cos\left(2\left(\omega t + \pi/6 + \alpha_v^\star\right)\right) \\ \cos\left(2\left(\omega t - \pi/2 + \alpha_v^\star\right)\right) \\ \cos\left(2\left(\omega t + 5\pi/6 + \alpha_v^\star\right)\right) \end{bmatrix}, \tag{29}$$

where the negative sign indicates the inductive mode while the positive sign is for the capacitive mode. Variable $Z_0^\star$ is the mean square-capacitor-voltage, i.e., $Z_0^\star = \left(z_{\Sigma-ab}^\star + z_{\Sigma-bc}^\star + z_{\Sigma-ca}^\star\right)/3$. Variable $S^\star = (3/2)\hat{V}^\star\left(\hat{I}^\star/\sqrt{3}\right)$ denotes the apparent power at the converter side, with $\hat{V}^\star$ and $\hat{I}^\star/\sqrt{3}$ as the amplitude of the fundamental converter voltage and arm current, respectively. Angle $\alpha_v^\star$ models the system losses, and corresponds to the phase-shift betwen the line-to-line PCC voltages and the converter voltages.

As discussed in [2], [11], it is convenient in the LC-StatComs to have a reference for $Z_0^\star$ that takes into account both normal and over-load operating conditions. The reason is to ensure that the voltages across the capacitors have a preset maximum value at $V_{C-\max}^\star$ for any reactive power reference below the nominal value ($I_q^\star \leq I_{q,n}$); and ensuring a preset minimum value at $V_{C-\min}^\star$ for over-load conditions ($I_q^\star > I_{q,n}$). Consequently, according to (29), the reference for $Z_0^\star$ taking into account both operating conditions corresponds to [2]:

$$Z_0^\star = \begin{cases} \frac{1}{2n}\left(nV_{C-\max}^\star\right)^2 - \frac{S^\star}{6\omega_g C}, & \text{if } I_q^\star \leq I_{q,n} \\ \frac{1}{2n}\left(nV_{C-\min}^\star\right)^2 + \frac{S^\star}{6\omega_g C}, & \text{if } I_q^\star > I_{q,n}. \end{cases} \tag{30}$$

Once the cluster voltage references $v_{\Sigma-x}^\star$ and the converter voltage references $v_x^\star$ are known, the control reference $\delta_x^\star$ for each CHB is calculated as

$$\delta_x^\star = v_x^\star / v_{\Sigma-x}^\star. \tag{31}$$

3) Outer Control Loop - Dynamic References Generation: It is important to note that the above-mentioned static references consider a set of nominal parameters for capacitances, inductances, and resistances. Uncertainty in converter parameters can provide an incorrect reference to track by the MPC. Adding an outer loop represents a common approach in StatCom control that shapes the static references in order to provide a set of correct references [15]–[18]. Unlike the conventional StatCom outer loop control schemes, where the capacitor voltages are used as the variables to regulate, in

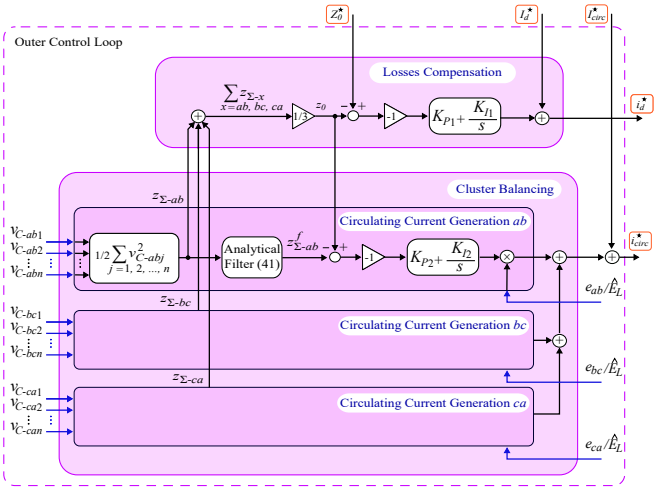

Fig. 4. Block diagram of the "Outer Control Loop" using the square-sum-capacitor-voltages.

the LC-StatComs it is necessary to use the square-capacitor-voltages [14], i.e.,

$$z_{C-xj} = \frac{1}{2} v_{C-xj}^2, \text{ and } z_{\Sigma-x} = \frac{1}{2} \sum_{j \in \mathcal{J}} v_{C-xj}^2. \tag{32}$$

In addition to this variable change, usual filtering schemes that appear in the outer control loop of the conventional StatComs have to be avoided in the LC-StatComs, since the capacitor voltage dynamics are much faster. This implies the use of analytic feedforward filtering techniques [1], [8].

Consequently, the outer control loop that provides a correct reference trajectory must change with respect to the conventional StatCom outer control loop. Specifically, Fig. 4 depicts the proposed "Outer Control Loop (Losses Compensation & Cluster Balancing)". Next, the importance of using the square-capacitor-voltages is discussed.

The dynamics of the cluster voltages $v_{\Sigma-x}$, according to (4), can be written as the following power relationship:

$$p_x = -\frac{C}{n} v_{\Sigma-x} \frac{dv_{\Sigma-x}}{dt}, \text{ with } p_x = v_x i_{arm-x}, \tag{33}$$

whose linearisations arround the equilibrium trajectory $V_{\Sigma-x}$ corresponds to

$$\tilde{p}_x \approx -\frac{C}{n} V_{\Sigma-x} \frac{d\tilde{v}_{\Sigma-x}}{dt} - \frac{C}{n} \tilde{v}_{\Sigma-x} \frac{dV_{\Sigma-x}}{dt}, \tag{34}$$

where the bilinear terms have been considered negligible.

Obviously, in the conventional StatComs, the term $\frac{dV_{\Sigma-x}}{dt}$ is assumed to be zero, i.e., $V_{\Sigma-x}$ is assumed constant due to the large capacitances used, yielding a power-to-voltage relationship independent of the operating conditions. Therefore, since the term $\frac{dV_{\Sigma-x}}{dt}$ cannot be neglected in the LC-StatComs, considering the power-to-voltage transfer function as

$$\frac{\tilde{V}_{\Sigma-x}(s)}{\tilde{P}_x(s)} = -\frac{1}{C/n\, V_{\Sigma-x} s}, \tag{35}$$

is not appropriate.

On the other hand, by using the square-sum-capacitor-voltages (32), where the variable change $(C/n)\, v_{\Sigma-x} \dot{v}_{\Sigma-x} = C \dot{z}_{\Sigma-x}$ is used in (33), the dc-side relationship becomes linear and independent of the operating conditions, i.e.,

$$\frac{\tilde{Z}_{\Sigma-x}(s)}{\tilde{P}_x(s)} = -\frac{1}{sC}, \tag{36}$$

which greatly simplifies the control design.

According to Fig. 4, $i_d^\star$ is calculated by regulating the mean square-capacitor-voltage, that is, $z_0 = (z_{\Sigma-ab} + z_{\Sigma-bc} + z_{\Sigma-ca})/3$, to the static reference $Z_0^\star$ (30), so that the system losses are compensated. Namely, $i_d^\star$ is the output of a proportional-integral (PI) component plus static reference $I_d^\star$ (26), i.e.,

$$i_d^\star = \left(K_{P1} \tilde{z}_0 + K_{I1} \int \tilde{z}_0 dt \right) + I_d^\star, \tag{37}$$

being the regulation error $\tilde{z}_0$,

$$\tilde{z}_0 = z_0 - Z_0^\star, \tag{38}$$

where $I_d^\star$, given in (26), has been added to the controller output to minimise control effort.

According to Fig. 4 and (36), choosing

$$K_{P1} = \frac{3C}{\hat{E}_L/\sqrt{2}} \frac{8}{T_{r1}}, \quad K_{I1} = \frac{3C}{\hat{E}_L/\sqrt{2}} \frac{16}{T_{r1}^2}, \tag{39}$$

yields a critically damped closed-loop response with a settling time of approximately T_{r1}.

According to Fig. 4, $i_{circ}^\star$ is calculated by regulating the filtered component of each square-sum-capacitor-voltages, namely $z_{\Sigma-ab}^f$, $z_{\Sigma-bc}^f$, $z_{\Sigma-ca}^f$, towards the mean square-capacitor-voltage z_0, so that the energy of the capacitors is balanced between the converter phase-arms. Particularly, the filtered square-sum-capacitor-voltages are calculated as follows,

$$z_{\Sigma-x}^f = z_{\Sigma-x} - \Delta z_{\Sigma-x}^\star, \tag{40}$$

with $\Delta z_{\Sigma-x}^\star$ referring to the twice fundamental harmonic component, i.e.,

$$\Delta z_{\Sigma-x}^\star = z_{\Sigma-x}^\star - Z_0^\star, \tag{41}$$

with $z_{\Sigma-x}^\star$ according to (29).

According to [15], injecting a circulating current with a fundamental frequency component, generates active power capable of balancing the energy of the capacitors between phases. Specifically, $i_{circ}^\star$ to achieve cluster balance corresponds to

$$i_{circ}^\star = \sum_{x \in \mathcal{X}} \left(K_{P2} \tilde{z}_{\Sigma-x}^f + K_{I2} \int \tilde{z}_{\Sigma-x}^f dt \right) \frac{e_x}{\hat{E}_L} + I_{circ}^\star, \tag{42}$$

being $\tilde{z}_{\Sigma-x}^f$ the regulation error of the filtered square-sum-capacitor-voltages, i.e.,

$$\tilde{z}_{\Sigma-x}^f = z_{\Sigma-x}^f - z_0. \tag{43}$$

Note that the line-to-line PCC voltages e_{ab}, e_{bc}, e_{ca} modulate the PI outputs, i.e., $K_{P2} \tilde{z}_{\Sigma-x}^f + K_{I2} \int \tilde{z}_{\Sigma-x}^f dt$. Consequently, the product between each fundamental circulating current in

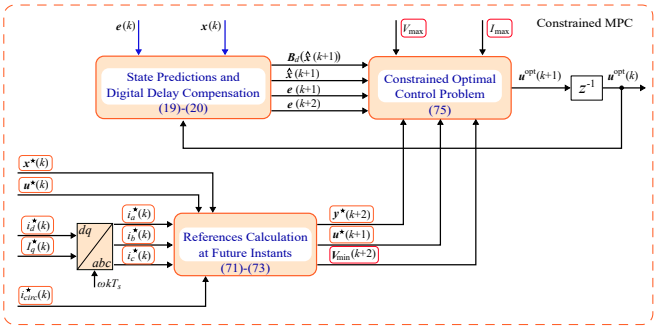

Fig. 5. Block diagram of the "Constrained MPC".

(42) and the converter voltages v_{ab}, v_{bc}, v_{ca}, leads to an active power distribution among the phases that steers each $z^f_{\Sigma-x}$ in the correct direction to balance the cluster voltages.

According to the experimental results, where the control action provided by the "Cluster Balancing" sub-block controller, when the cluster voltages are balanced, is zero, a proportional controller satisfies the control objective [30]. Therefore, according to Fig. 4 and (36), choosing

$$K_{P2} = \frac{2C}{\hat{E}_L}\frac{4}{T_{r2}}, \quad K_{I2} = 0, \tag{44}$$

yields a first-order closed-loop response with a settling time of approximately T_{r2}.

C. Predictor and Digital Delay Compensation

Fig. 5 depicts the structure of the "Constrained MPC" block. The optimisation is performed over open-loop predictions, which are based on the accurate discrete-time model of the LC-StatCom discussed in the previous section, and defined in (19)-(20).

Obviously, in the prediction of $\boldsymbol{x}$ at instant $k+1$, i.e., $\hat{\boldsymbol{x}}(k+1)$, according to (19), the term $\boldsymbol{B}_d(\boldsymbol{x}(k))$ appears. According to (20), and due to the bilinear nature of the converter, the term $\boldsymbol{B}_d(\boldsymbol{x}(k))$ depends on the summation of state intersamples $\boldsymbol{x}(k+mT_s/M)$, which in turn, depend on $\boldsymbol{u}(k)$. As $\boldsymbol{u}(k)$ is unknown at time instant k, $\boldsymbol{u}^{\text{opt}}(k-1)$ is assumed as its best estimation. This consideration is only valid for slow enough variations of the control signal $\boldsymbol{u}(k)$. This is related to the control bandwidth, which in turn is related to the penalisation of the control signal within the cost function. Considering the true value of $\boldsymbol{u}(k)$ in the intersample terms $\boldsymbol{x}(k+mT_s/M)$, would result in a nonlinear dependence on $\boldsymbol{u}(k)$, which would prevent the use of a QP approach in the optimisation block, which will be explained in the next subsection.

Also, the proposed control takes into account the time delay required for A/D conversion plus control calculations when implementing a digital controller [31]. This means that once the state $\boldsymbol{x}$ and voltage $\boldsymbol{e}$ are measured at instant k, it is not possible to calculate $\boldsymbol{u}(k)$ instantly. In the sequel, this delay is considered to be a sample time T_s. Nevertheless, the upcoming control $\boldsymbol{u}(k+1)$ can be calculated. This means that at instant k the applied control input to the converter is well known as it was calculated in the previous sampling period, i.e., between $k-1$ and k. As a consequence, using the proposed predictor, the state $\boldsymbol{x}$ at $k+1$ can be predicted as $\hat{\boldsymbol{x}}(k+1)$. Similarly, the rotation matrix $\boldsymbol{R}_\omega$ can be used to exactly calculate the voltage $\boldsymbol{e}$ at $k+1$ as $\boldsymbol{e}(k+1) = \boldsymbol{R}_\omega^M \boldsymbol{e}(k)$. Hence, the state trajectory $\boldsymbol{x}$ at instant $k+2$ can be predicted as

$$\hat{\boldsymbol{x}}(k+2) = \boldsymbol{A}_d\hat{\boldsymbol{x}}(k+1) + \boldsymbol{B}_d(\hat{\boldsymbol{x}})\,\boldsymbol{u}(k+1) + \boldsymbol{W}_d\boldsymbol{e}(k+1), \tag{45}$$

with $\boldsymbol{B}_d(\hat{\boldsymbol{x}}) = \boldsymbol{B}_d(\hat{\boldsymbol{x}}(k+1))$, and matrices as in (20).

D. Cost Function and Constraints

The cost function constitutes one of the key elements in any MPC scheme, since it establishes the desired behaviour of the system during transient and steady-state operation.

The proposed cost function J consists of three terms, namely,

$$J = J_1 + J_2 + J_3. \tag{46}$$

The first one, denoted as J_1, penalises the predicted tracking error of the system output, that is, the difference between the output reference $\boldsymbol{y}^\star$ and the predicted output $\hat{\boldsymbol{y}}$. This term is given by

$$J_1 = \|\tilde{\boldsymbol{y}}(k+2)\|^2_{\boldsymbol{Q}_y} = \tilde{\boldsymbol{y}}(k+2)^T\,\boldsymbol{Q}_y\tilde{\boldsymbol{y}}(k+2), \tag{47}$$

where

$$\tilde{\boldsymbol{y}}(k) = \hat{\boldsymbol{y}}(k) - \boldsymbol{y}^\star(k). \tag{48}$$

The considered output vector corresponds to

$$\boldsymbol{y} = [p\ q\ i_{circ}\ v_{\Sigma-ab}\ v_{\Sigma-bc}\ v_{\Sigma-ca}]^T = \boldsymbol{C}\boldsymbol{x}, \tag{49}$$

where the output matrix $\boldsymbol{C}$ corresponds to

$$\boldsymbol{C}(k) = \begin{bmatrix} \boldsymbol{C}_{11}(k) & \boldsymbol{0}_{2\times4} \\ \boldsymbol{0}_{4\times2} & \boldsymbol{I}_4 \end{bmatrix}, \tag{50}$$

with submatrix $\boldsymbol{C}_{11}$ as

$$\boldsymbol{C}_{11} = \begin{bmatrix} e_a - e_c & e_b - e_c \\ \frac{1}{\sqrt{3}}(-e_a + 2e_b - e_c) & \frac{1}{\sqrt{3}}(-2e_a + e_b + e_c) \end{bmatrix}. \tag{51}$$

It can be noted that matrix $\boldsymbol{C}$ is time-varying. Note that the weighting matrix $\boldsymbol{Q}_y$ in (47) must be symmetric and positive semidefinite, i.e., $\boldsymbol{Q}_y \in \mathbb{S}_{\geq 0}$. Thus, the weighting matrix $\boldsymbol{Q}_y$ can be defined as:

$$\boldsymbol{Q}_y = \text{diag}\left(\lambda_p,\ \lambda_q,\ \lambda_{i_{circ}},\ \lambda_{v_{\Sigma-ab}},\ \lambda_{v_{\Sigma-bc}},\ \lambda_{v_{\Sigma-ca}}\right). \tag{52}$$

As in [32], [33], when directly controlling the instantaneous real and imaginary powers, the penalty on the corresponding two error tracking terms can be chosen equal, that is, $\lambda_p = \lambda_q$.

Using the prediction model in (45), cost function (47) can be rewritten as a quadratic function in terms of the control input $\boldsymbol{u}(k+1)$.

It is also important to add a term in the cost function that penalises the tentative control input $\boldsymbol{u}$ with respect to its steady-state reference value $\boldsymbol{u}^\star$, i.e., the control effort, which

can provide a certain degree of robustness and stability [22], [34], [35].

Based on the previous reasoning, a second term in the cost function is added, which is denoted as J_2. This term is given by

$$J_2 = \|\tilde{\boldsymbol{u}}\,(k+1)\|^2_{\boldsymbol{R}} = \tilde{\boldsymbol{u}}\,(k+1)^T\,\boldsymbol{R}\tilde{\boldsymbol{u}}\,(k+1)\,, \tag{53}$$

where

$$\tilde{\boldsymbol{u}}\,(k) = \boldsymbol{u}\,(k) - \boldsymbol{u}^\star\,(k)\,. \tag{54}$$

Note that the weighting matrix $\boldsymbol{R}$ must be symmetric positive definite, i.e., $\boldsymbol{R} \in \mathbb{S}_{>0}$. Thus, the weighting matrix $\boldsymbol{R}$ can be defined as:

$$\boldsymbol{R} = \lambda_u \boldsymbol{I}_3. \tag{55}$$

Note that cost function (53) is a quadratic function in terms of control input $\boldsymbol{u}\,(k+1)$.

One of the most attractive features of the MPC is its ability to deal with constraints in the optimal control determination.

One constraint is the modulation limits, i.e.,

$$-\boldsymbol{U}_3 \preceq \boldsymbol{u}\,(k+1) \preceq \boldsymbol{U}_3, \tag{56}$$

where $\boldsymbol{U}_3$ is a column vector of ones. This constraint defines a strict physical limitation of the converter.

Now, constraints on the arm currents and capacitor voltages are addressed. Upper and lower bounds at I_{max} and I_{min} are placed for the arm currents, while V_{max} and V_{min} define the upper and lower bounds for the cluster voltages. By aggregating the previous bounds in vectors, and using $I_{\text{min}} = -I_{\text{max}}$, yields

$$\begin{array}{l} -I_{\text{max}}\boldsymbol{U}_3 \preceq \boldsymbol{C}_1\hat{\boldsymbol{x}}\,(k+2) \preceq I_{\text{max}}\boldsymbol{U}_3 \\ \boldsymbol{V}_{\text{min}}\,(k+2) \preceq \boldsymbol{C}_2\hat{\boldsymbol{x}}\,(k+2) \preceq V_{\text{max}}\boldsymbol{U}_3, \end{array} \tag{57}$$

with matrices corresponding to

$$\boldsymbol{C}_1 = \begin{bmatrix} 1/3 & -1/3 & 1 & 0 & 0 & 0 \\ 1/3 & 2/3 & 1 & 0 & 0 & 0 \\ -2/3 & -1/3 & 1 & 0 & 0 & 0 \end{bmatrix}, \tag{58}$$

$$\boldsymbol{C}_2 = \begin{bmatrix} \boldsymbol{0}_3 & \boldsymbol{I}_3 \end{bmatrix}, \tag{59}$$

and where the lower bound for the cluster voltages is time-varying

$$\boldsymbol{V}_{\text{min}}\,(k) = \begin{bmatrix} |v^\star_{ab}\,(k)| \\ |v^\star_{bc}\,(k)| \\ |v^\star_{ca}\,(k)| \end{bmatrix}. \tag{60}$$

Note that references $\boldsymbol{y}^\star = \boldsymbol{C}\boldsymbol{x}^\star$ in (47) must be accordingly constrained to adhere to the operational limits, i.e.,

$$\begin{array}{l} -I_{\text{max}}\boldsymbol{U}_3 \preceq \boldsymbol{C}_1\boldsymbol{x}^\star\,(k+2) \preceq I_{\text{max}}\boldsymbol{U}_3 \\ \boldsymbol{V}_{\text{min}}\,(k+2) \preceq \boldsymbol{C}_2\boldsymbol{x}^\star\,(k+2) \preceq V_{\text{max}}\boldsymbol{U}_3. \end{array} \tag{61}$$

It is important to note that the lower limit on the capacitor voltages in (57), and the modulation limits in (56), are different. If only (56) is imposed, the capacitor voltages are free to vary outside the envelopes (57) to a certain extent, and only the converter voltages should be chosen below the present cluster voltage values so as to minimise the objective cost function. The constraint in (57) creates a constraint on the envelope, meaning that no matter what power reference is desired to track, it should be impossible to drive the capacitor voltages out of the envelopes.

Using the prediction model in (45), the state constraints in (57) can be mapped into input constraints in the following way,

$$\boldsymbol{A}_c\boldsymbol{u}\,(k+1) \preceq \boldsymbol{b}_c, \tag{62}$$

with constraints matrix $\boldsymbol{A}_c \in \mathbb{R}^{12\times 3}$ and constraints vector $\boldsymbol{b}_c \in \mathbb{R}^{12}$ corresponding to

$$\boldsymbol{A}_c = \begin{bmatrix} \boldsymbol{A}_{c1} \\ \boldsymbol{A}_{c2} \\ \boldsymbol{A}_{c3} \\ \boldsymbol{A}_{c4} \end{bmatrix} = \begin{bmatrix} \boldsymbol{C}_1\boldsymbol{B}_d\,(\hat{\boldsymbol{x}}) \\ -\boldsymbol{C}_1\boldsymbol{B}_d\,(\hat{\boldsymbol{x}}) \\ \boldsymbol{C}_2\boldsymbol{B}_d\,(\hat{\boldsymbol{x}}) \\ -\boldsymbol{C}_2\boldsymbol{B}_d\,(\hat{\boldsymbol{x}}) \end{bmatrix}, \tag{63}$$

$$\boldsymbol{b}_c = \begin{bmatrix} \boldsymbol{b}_{c1} \\ \boldsymbol{b}_{c2} \\ \boldsymbol{b}_{c3} \\ \boldsymbol{b}_{c4} \end{bmatrix} = \begin{bmatrix} I_{\text{max}}\boldsymbol{U}_3 - \boldsymbol{C}_1\boldsymbol{A}_d\hat{\boldsymbol{x}}\,(k+1) - \boldsymbol{C}_1\boldsymbol{W}_d\boldsymbol{e}\,(k+1) \\ I_{\text{max}}\boldsymbol{U}_3 + \boldsymbol{C}_1\boldsymbol{A}_d\hat{\boldsymbol{x}}\,(k+1) + \boldsymbol{C}_1\boldsymbol{W}_d\boldsymbol{e}\,(k+1) \\ V_{\text{max}}\boldsymbol{U}_3 - \boldsymbol{C}_2\boldsymbol{A}_d\hat{\boldsymbol{x}}\,(k+1) - \boldsymbol{C}_2\boldsymbol{W}_d\boldsymbol{e}\,(k+1) \\ -\boldsymbol{V}_{\text{min}}\,(k+2) + \boldsymbol{C}_2\boldsymbol{A}_d\hat{\boldsymbol{x}}\,(k+1) + \boldsymbol{C}_2\boldsymbol{W}_d\boldsymbol{e}\,(k+1) \end{bmatrix}, \tag{64}$$

with $\boldsymbol{B}_d\,(\hat{\boldsymbol{x}}) = \boldsymbol{B}_d\,(\hat{\boldsymbol{x}}\,(k+1))$. Note that $\boldsymbol{A}_c$ and $\boldsymbol{b}_c$ are time-varying, and hence they need to be calculated online at each control period T_s.

To avoid nonfeasibility issues that can break the program in the controller implementation, the hard constraint in (62) is relaxed by adding a vector of surplus variables (or negative slack variable) in the optimisation problem as,

$$\begin{bmatrix} \boldsymbol{A}_{c1} \\ \boldsymbol{A}_{c2} \\ \boldsymbol{A}_{c3} \\ \boldsymbol{A}_{c4} \end{bmatrix} \boldsymbol{u} \preceq \begin{bmatrix} \boldsymbol{b}_{c1} \\ \boldsymbol{b}_{c2} \\ \boldsymbol{b}_{c3} \\ \boldsymbol{b}_{c4} \end{bmatrix} + \begin{bmatrix} \boldsymbol{\xi}_i \\ \boldsymbol{\xi}_i \\ \boldsymbol{\xi}_v \\ \boldsymbol{\xi}_v \end{bmatrix}, \tag{65}$$

where the argument of $\boldsymbol{u}$, $\boldsymbol{\xi}_i$, and $\boldsymbol{\xi}_v$ is suppressed for brevity, being

$$\begin{array}{l} \boldsymbol{\xi}_i = \begin{bmatrix} \xi_i & \xi_i & \xi_i \end{bmatrix}^T \in \mathbb{R}^3_{\geq 0} \\ \boldsymbol{\xi}_v = \begin{bmatrix} \xi_v & \xi_v & \xi_v \end{bmatrix}^T \in \mathbb{R}^3_{\geq 0} \end{array} \tag{66}$$

column vectors that group the nonnegative surplus terms for the corresponding states. Physically, the surplus terms $\boldsymbol{\xi}_i$, $\boldsymbol{\xi}_v$ represent how much the states exceed their bounds. Therefore, the surplus terms $\boldsymbol{\xi}_i$, $\boldsymbol{\xi}_v$ need to be strongly penalised within the cost function so that the soft constraints (65) keep the state variables almost as strictly within their bounds as hard constraints (62) do, while avoiding potential numerical and nonfeasibility issues.

Therefore, the new optimisation variable is defined as

$$\boldsymbol{\mu}\,(k) = \begin{bmatrix} \boldsymbol{u}\,(k) \\ \boldsymbol{\xi}_i\,(k) \\ \boldsymbol{\xi}_v\,(k) \end{bmatrix} \in \mathbb{R}^9. \tag{67}$$

Consequently, the hard constraint (56), the soft constraint (65), and the nonnegativity condition for the surplus terms (66), can

be groupped as the following equivalent set of linear inequality constraints on the optimisation variable $\boldsymbol{\mu}$:

$$\left[\begin{array}{ccc} \boldsymbol{A}_{c1} & -\boldsymbol{I}_3 & \boldsymbol{0}_3 \\ \boldsymbol{A}_{c2} & -\boldsymbol{I}_3 & \boldsymbol{0}_3 \\ \boldsymbol{A}_{c3} & \boldsymbol{0}_3 & -\boldsymbol{I}_3 \\ \boldsymbol{A}_{c4} & \boldsymbol{0}_3 & -\boldsymbol{I}_3 \\ -\boldsymbol{I}_3 & \boldsymbol{0}_3 & \boldsymbol{0}_3 \\ \boldsymbol{I}_3 & \boldsymbol{0}_3 & \boldsymbol{0}_3 \\ \boldsymbol{0}_3 & -\boldsymbol{I}_3 & \boldsymbol{0}_3 \\ \boldsymbol{0}_3 & \boldsymbol{0}_3 & -\boldsymbol{I}_3 \end{array}\right] \boldsymbol{\mu} \preceq \left[\begin{array}{c} \boldsymbol{b}_{c1} \\ \boldsymbol{b}_{c2} \\ \boldsymbol{b}_{c3} \\ \boldsymbol{b}_{c4} \\ \boldsymbol{U}_3 \\ \boldsymbol{U}_3 \\ \boldsymbol{0}_{3\times 1} \\ \boldsymbol{0}_{3\times 1} \end{array}\right], \tag{68}$$

which ensures that i) the capacitor voltages and arm currents are maintained within desired envelopes (first 4 rows), that ii) the modulation functions are within their physical limits (rows 5 and 6), and that iii) the algorithm does not try to make $\boldsymbol{\xi}_i$, $\boldsymbol{\xi}_v$ negative (last two rows).

As the surplus variables are desired to be minimised, the following term needs to be added to the cost function

$$J_3 = \|\boldsymbol{\xi}_i\|^2_{\boldsymbol{S}_i} + \|\boldsymbol{\xi}_v\|^2_{\boldsymbol{S}_v}. \tag{69}$$

Note that the weighting matrices $\boldsymbol{S}_i$ and $\boldsymbol{S}_v$ are symmetric positive definite, i.e., $\boldsymbol{S}_i \in \mathbb{S}_{>0}$ and $\boldsymbol{S}_v \in \mathbb{S}_{>0}$. Thus, the weighting matrices $\boldsymbol{S}_i$ and $\boldsymbol{S}_v$ can be defined as:

$$\boldsymbol{S}_i = \lambda_{\xi_i}\boldsymbol{I}_3, \quad \boldsymbol{S}_v = \lambda_{\xi_v}\boldsymbol{I}_3. \tag{70}$$

To ensure that the soft constraints (65) are appropriately treated, the penalties λ_{ξ_i} and λ_{ξ_v} are chosen large enough.

E. Calculation of Future Reference Values

Cost function $J_1 + J_2$ ((47) and (53)) depends on future values of the state reference and control input reference. Moreover, the lower limit (60) for the capacitor voltage constraints (57) also depend on future values of the references. Obviously, the values of the state reference $\boldsymbol{x}^\star$ and the control reference $\boldsymbol{u}^\star$ at future instants are unknown at the instant of measurement k, and a calculation is needed.

The concept of the rotation matrix $\boldsymbol{R}_\omega$ (21) can be used here to calculate future values of the reference signals. For example, the injected StatCom current references at instant $k+1$ can be calculated as follows:

$$\left[\begin{array}{c} i_a^\star(k+1) \\ i_b^\star(k+1) \\ i_c^\star(k+1) \end{array}\right] = \boldsymbol{R}_\omega^M \left[\begin{array}{c} i_a^\star(k) \\ i_b^\star(k) \\ i_c^\star(k) \end{array}\right]. \tag{71}$$

Similarly, the converter voltage references (85) at future instants, can be calculated as follows:

$$\left[\begin{array}{c} v_{ab}^\star(k+1) \\ v_{bc}^\star(k+1) \\ v_{ca}^\star(k+1) \end{array}\right] = \boldsymbol{R}_\omega^M \left[\begin{array}{c} v_{ab}^\star(k) \\ v_{bc}^\star(k) \\ v_{ca}^\star(k) \end{array}\right]. \tag{72}$$

Regarding the future values for the cluster voltage references, it is easier to calculate them indirectly through the square-sum-capacitor-voltage references (29). The mean square-capacitor-voltage $Z_0^\star$ is constant in time (30), whereas the twice fundamental harmonic $\Delta z_{\Sigma-x}^\star$ (41) at instant $k+1$ can be calculated as:

$$\left[\begin{array}{c} \Delta z_{\Sigma-ab}^\star(k+1) \\ \Delta z_{\Sigma-bc}^\star(k+1) \\ \Delta z_{\Sigma-ca}^\star(k+1) \end{array}\right] = \boldsymbol{R}_{-2\omega}^M \left[\begin{array}{c} \Delta z_{\Sigma-ab}^\star(k) \\ \Delta z_{\Sigma-bc}^\star(k) \\ \Delta z_{\Sigma-ca}^\star(k) \end{array}\right], \tag{73}$$

with $\boldsymbol{R}_{-2\omega}$ being a rotation matrix that considers the double frequency and negative sequence of the square-sum-capacitor-voltages, i.e.,

$$\boldsymbol{R}_{-2\omega} = \boldsymbol{T}^\dagger_{\alpha\beta} \left[\begin{array}{cc} \cos\left(-2\omega\frac{T_s}{M}\right) & -\sin\left(-2\omega\frac{T_s}{M}\right) \\ \sin\left(-2\omega\frac{T_s}{M}\right) & \cos\left(-2\omega\frac{T_s}{M}\right) \end{array}\right] \boldsymbol{T}_{\alpha\beta}. \tag{74}$$

Consequently, the cluster voltage references at future instants can be calculated using (28). Subsequently, $\boldsymbol{u}^\star$ at future instants is calculated using (31).

F. Constrained Optimisation Problem

Combining the cost function in (47), (53), (69), the constraints in (68), and the new optimisation variable $\boldsymbol{\mu}$ in (67), the initial optimisation problem depicted in (23) becomes:

$$\begin{array}{l} \boldsymbol{\mu}^{\text{opt}}(k+1) = \arg \underset{\boldsymbol{\mu}}{\text{minimise}} \quad (1/2)\,\boldsymbol{\mu}^T\boldsymbol{H}\boldsymbol{\mu} + \boldsymbol{f}^T\boldsymbol{\mu} \\ \text{subject to (68)} \end{array}, \tag{75}$$

where the argument of $\boldsymbol{\mu}$ is suppressed for brevity, and the Hessian matrix $\boldsymbol{H}$ and the gradient vector $\boldsymbol{f}$ correspond to

$$\boldsymbol{H} = \left[\begin{array}{ccc} \boldsymbol{H}_{11} & \boldsymbol{0}_3 & \boldsymbol{0}_3 \\ \boldsymbol{0}_3 & \boldsymbol{S}_i & \boldsymbol{0}_3 \\ \boldsymbol{0}_3 & \boldsymbol{0}_3 & \boldsymbol{S}_v \end{array}\right], \quad \boldsymbol{f} = \left[\begin{array}{c} \boldsymbol{f}_1 \\ \boldsymbol{0}_{3\times 1} \\ \boldsymbol{0}_{3\times 1} \end{array}\right], \tag{76}$$

where the Hessian submatrix $\boldsymbol{H}_{11}$ and gradient vector $\boldsymbol{f}_1$ correspond to

$$\begin{array}{l} \boldsymbol{H}_{11} = \boldsymbol{B}_d(\hat{\boldsymbol{x}})^T \boldsymbol{Q}_x \boldsymbol{B}_d(\hat{\boldsymbol{x}}) + \lambda_u \boldsymbol{I}_3, \\ \boldsymbol{f}_1 = \boldsymbol{B}_d(\hat{\boldsymbol{x}})^T \boldsymbol{Q}_x \\ (\boldsymbol{A}_d\hat{\boldsymbol{x}}(k+1) - \boldsymbol{x}^\star(k+2) + \boldsymbol{W}_d\boldsymbol{e}(k+1)) \\ -\lambda_u \boldsymbol{u}^\star(k+1), \end{array} \tag{77}$$

with $\boldsymbol{B}_d(\hat{\boldsymbol{x}}) = \boldsymbol{B}_d(\hat{\boldsymbol{x}}(k+1))$, and $\boldsymbol{Q}_x = \boldsymbol{Q}_x(k+2)$, where

$$\boldsymbol{Q}_x(k) = \boldsymbol{C}(k)^T \boldsymbol{Q}_y \boldsymbol{C}(k). \tag{78}$$

Note that $\boldsymbol{H}$ and $\boldsymbol{f}$ are time-varying, and hence they need to be calculated online at each control period T_s.

As the function to minimise is quadratic, and the optimisation is subject to linear inequality constraints, the resulting optimisation problem (75) constitutes a QP problem.

The result of the optimisation is the sequence of optimal control inputs $\boldsymbol{u}$ and surplus terms $\boldsymbol{\xi}_i$, $\boldsymbol{\xi}_v$, according to (67). The first three elements of the optimisation variable correspond to $\boldsymbol{u}^{\text{opt}} = \left[\begin{array}{ccc} \delta_{ab}^{\text{opt}} & \delta_{bc}^{\text{opt}} & \delta_{ca}^{\text{opt}} \end{array}\right]^T$, which are implemented at instant k and sent to the "Modulation & Interbridge Balancing Control" block.

IV. Experimental Results

With the purpose of assessing the proposed constrained MPC approach to control three-phase LC-StatComs, both in steady-state and during transients, this section describes the measurements that illustrate the controller behaviour concerning its ability to provide fast transient responses while fulfilling the design constraints.

TABLE I
EXPERIMENTAL SYSTEM PARAMETERS

Parameter	Value
Nominal line-to-line PCC voltage amplitude, $\hat{E}_{L,n}$	$30\sqrt{2}\sqrt{3}$ V (1 p.u.)
Grid nominal power, $S_{g,n}$	636 VA (1 p.u.)
Grid angular frequency, ω_g	20π rad/s
Individual switch switching frequency, f_{sw}	20 kHz
Controller Sampling period, T_s	500 μs
Maximum capacitor voltage reference, $V^{\star}_{C-\max}$	$1.3\hat{E}_{L,n}/n =$ 95.5 V
Capacitance per H-bridge, C	0.96 mF ($r_n = 0.6$)
Filter inductances, L L_{arm}	5 mH (0.075 p.u.) 5 mH (0.075 p.u.)
Parasitic resistances, R R_{arm}	150 mΩ (0.035 p.u.) 150 mΩ (0.035 p.u.)

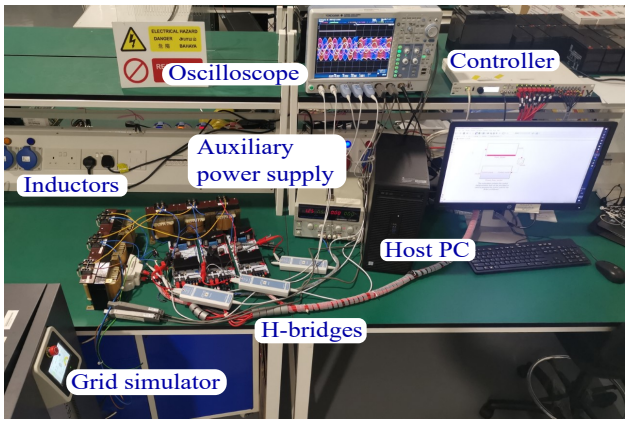

Fig. 6. Experimental system setup.

A. System and Control Parameters

The LC-StatCom laboratory prototype is connected to a 30-V grid, and it has a rated apparent power of approximately 700 VA. Table I summarises the system parameters and Fig. 6 shows the experimental setup. The inductors have been sized to provide a rated voltage drop of approximately 10% between the converter ac-side voltage and the PCC voltage.

The PCC voltage is provided by a GE&EL 15 kVA CINERGIA grid emulator. In this setup, three IMPERIX PEH2015 H-bridge converters were used to construct a three-level LC-StatCom with delta configuration, with the dc-link capacitor of $C = 0.96$ mF. The capacitors operate at a peak voltage reference of $V^{\star}_{C-\max} = 95.5$ V. The value of the dc-link capacitance C has been designed for a nominal low-frequency voltage ripple of 60%, i.e., $r_n = 0.6$ [36], according to

$$C = \frac{2S_n}{3n}\frac{1}{\omega_g V^{\star 2}_{C-\max} r_n\,(2-r_n)}, \tag{79}$$

with S_n as the rated converter power (corresponding to approximately 700 VA in the experimental setup).

The control functions were implemented in a B-Box RCP 3.0 board from IMPERIX. It is noted that the B-Box RCP has a dual-core DSP (2x ARM Cortex A9 1GHz, 1GB DDR3), in which the MPC controller is implemented with 2 kHz sampling. This means that the PWM inputs, i.e. the voltages corresponding to the duty cycles, are generated at a sample rate of 2 kHz. The PWM is implemented in a Kintex-grade FPGA (Xilinx Kintex 7 125K) with a time resolution of 4 ns, using a 20-kHz 32-bit triangular carrier. To solve the optimisation problem, an open-source convex QP solver, OSQP [37], [38], based on ADMM, was programmated. Predictions are calculated using the proposed predictor with $M = 6$ intersamples, and the maximum number of iterations of the OSQP solver has been set to 20, which represents approximately 90% of the available computational resources when using a sampling rate of $1/T_s = 2$ kHz.

The weighting factors used in the predictive controller to trade-off the different control objectives (according to (52) for the output error penalisation, to (55) for the control effort penalisation, and to (70) for the surplus variables) have the following values:

$$\begin{aligned} &\lambda_p = \lambda_q = 20/S^2_{g,n}, \quad \lambda_{i_{circ}} = 3/\left(\hat{I}_n/\sqrt{3}\right)^2, \\ &\lambda_{v_{\Sigma-ab}} = \lambda_{v_{\Sigma-bc}} = \lambda_{v_{\Sigma-ca}} = 0, \\ &\lambda_u = 1, \quad \lambda_{\xi_i} = \lambda_{\xi_v} = 10^6, \end{aligned} \tag{80}$$

with $S_{g,n} = 636$ VA and $\hat{I}_n = 10$ A according to Table I.

Regarding the block "Outer Control Loop (Losses Compensation & Cluster Balancing)" that provides dynamic references to the predictive control (as depicted in Fig. 4), the control parameters in (39) and (44) have been used for a response time of $T_{r1} = 2.5\,(2\pi/\omega_g)$ s in the "Losses Compensation" sub-block, and $T_{r2} = 1.5\,(2\pi/\omega_g)$ s in the "Cluster Balancing" sub-block. These parameter values show an excellent trade-off between overshoot and speed response of the expected active grid current component $i^{\star}_d$ and circulating current $i^{\star}_{circ}$.

B. Dynamic Performance

The operation of the proposed constrained predictive controller is tested under an abrupt change in the instantaneous imaginary power reference $q^{\star}$, from 80%-rated power capacitive-mode to 40%-rated power inductive-mode, and then a return to 80%-rated power capacitive-mode. Fig. 7 shows the experimental waveforms. The top capacitor voltage bound $V_{\max}$ is fixed at 40% over the nominal line-to-line PCC voltage, i.e., $V_{\max} = 1.4\hat{E}_{L,n}$, which corresponds to the state constraint in (57). This bound, which is indicated in Fig. 7(g) with a dashed line, is of paramount interest in the LC-StatComs because it allows one to reduce the capacitor size and simultaneously operate in a safe range that prevents overvoltages on capacitors and semiconductors. Current waveforms also remain within their prescribed bounds. The magnitude of the current bound is chosen to be $I_{\max} = 1.5\hat{I}_n/\sqrt{3}$, which corresponds to the state constraint in (57). The current bound has been chosen to protect the power semiconductor, thus limiting the peak arm current.

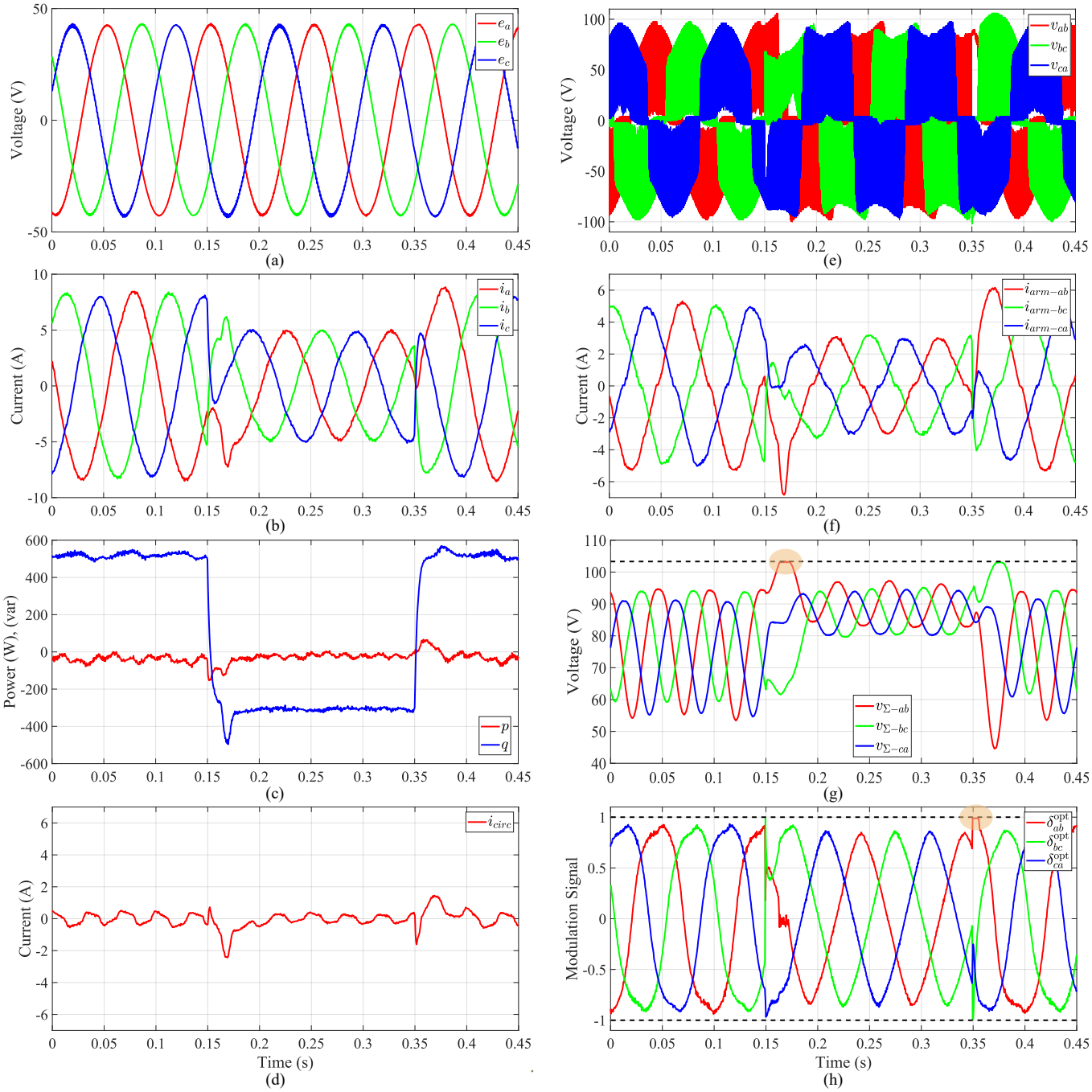

Fig. 7. Experimental waveforms during a sudden reactive power change from 80%-rated power capacitive-mode to 40%-rated power inductive-mode at $t = 0.15$ s, and vice versa at $t = 0.35$ s. (a) Line-to-neutral PCC voltages e_a, e_b, e_c, (b) injected StatCom currents i_a, i_b, i_c, (c) instantaneous powers p, q, (d) circulating current i_{circ}, (e) PWM converter voltages v_{ab}, v_{bc}, v_{ca}, (f) arm currents i_{arm-ab}, i_{arm-bc}, i_{arm-ca}, (g) capacitor voltages $v_{\Sigma-ab}$, $v_{\Sigma-bc}$, $v_{\Sigma-ca}$, and (h) optimal modulation signals δ_{ab}^{opt}, δ_{bc}^{opt}, δ_{ca}^{opt}.

It can be observed that the magnitude of the fundamental components of the converter voltages v_{ab}, v_{bc}, v_{ca}, Fig. 7(e), are in phase with their respective capacitor voltages $v_{\Sigma-ab}$, $v_{\Sigma-bc}$, $v_{\Sigma-ca}$, Fig. 7(g), when operating in the capacitive region, whilst the magnitude of the fundamental components are in counterphase with the capacitor voltages during inductive mode. It can be observed that the changes that occur in $t = 0.15\,\text{s}$ and $t = 0.35\,\text{s}$ are almost instantaneous. Also, it can be appreciated that due to the low capacitance used, the capacitor voltages present an oscillation (low-frequency ripple) above 50% of their dc values during capacitive operation.

It is worth noting that the transient response of the injected currents i_a, i_b, i_c and instantaneous powers p, q at $t = 0.15\,\text{s}$, as shown in Figs. 7(b) and (c), is very fast, with a settling time for the reactive power of less than one fifth of the fundamental period. It happens, despite the fact that the cluster voltage $v_{\Sigma-ab}$ is bounded by its top limit V_{max} at $t = 0.163\,\text{s}$ for one tenth of the fundamental period approximately, as illustrated in Fig. 7(g). It can be seen that the modulation signal δ_{ab}^{opt} is close to zero while $v_{\Sigma-ab} = V_{\text{max}}$ is bounded, as shown in Fig. 7(h), which is in agreement with the capacitor voltage dynamics in (4). Also note that when the cluster voltage $v_{\Sigma-ab}$ is bounded, the injected currents and instantaneous power, as shown in Figs. 7(b) and (c), deviate from their expected references. This result highlights the trade-off inherent with the proposed approach, i.e., the ability to constrain state variables causes some temporary tracking error in the output power and currents.

The transient response of the injected currents i_a, i_b, i_c and instantaneous powers p, q at $t = 0.35\,\text{s}$, as shown in Fig. 7(b) and (c), is also very fast, with a settling time for the reactive power of less than one tenth of the fundamental period. However, in this transient, state constraints (57) are not active. On the contrary, the constraint that limits the modulation signal δ_{ab}^{opt} in the range $[-1,\ 1]$ is active at $t = 0.35\,\text{s}$ for approximately one twentieth of the fundamental period, according to (56). This result demonstrates the MPC ability to constrain the inputs. Also, note that the modulation signal range can be modified by changing its bounds, according to (56).

Therefore, the experimental measures show fast transients and the capability of limiting the state variables and the inputs, which is of paramount importance in the LC-StatComs.

V. Complimentary Simulations

In this section, additional simulation results for a 36-MVA multilevel LC-StatCom with five submodules per phase are provided to demonstrate the effectiveness of the proposed constrained MPC to limit the individual capacitor voltages during transient operation when multiple submodules are used. The parameters of the simulated system are the same (in per-unit system) to those used in the experiment (given in Table I), but for a 6-kV 50-Hz grid. The system is simulated in the MATLAB/Simulink environment using a sampling rate of 10 kHz.

The block "Modulation & Interbridge Balancing Control" in Fig. 3 is implemented using a phase-shifted carrier pulse-width modulation (PSC-PWM) strategy [14] with 1 kHz carriers.

The waveforms for the case when $q^\star$ changes from 100%-rated power capacitive-mode to 50%-rated power inductive-mode at $t = 0.02\,\text{s}$ are shown in Fig. 8.

Similar to the experimental results, the cluster voltage $v_{\Sigma-ab}$ is bounded by its top limit V_{max} at $t = 0.021\,\text{s}$ for one fifth of the fundamental period approximately, as illustrated in Fig. 8(a). Consequently, the five individual capacitor voltages embedded in phase-arm ab are also bounded by their top limit V_{max}/n, as illustrated in Fig. 8(e). It can be seen that the optimal modulation signal δ_{ab}^{opt} calculated by the MPC is close to zero while $v_{\Sigma-ab} = V_{\text{max}}$, as shown in Fig. 8(f). While the capacitors voltages are temporarily bounded the currents do not follow the expected reference, as shown in Fig. 8(d), reaching the extreme case where the arm current i_{arm-ab} is bounded by its bottom limit I_{min} at $t = 0.021\,\text{s}$ for one fifth of the fundamental period approximately.

Above simulation results are in agreement with the experimental results shown in Fig. 7, thus corroborating that the proposed method can correctly work when multiple submodules are used.

For the sake of completeness, the LC-StatCom performance when using the proposed constrained MPC is compared to that obtained when using a more traditional control based on linear control. Specifically, the structure of the controller is exactly the same as that of the proposed MPC, which corresponds to Fig. 3, but the "Constrained MPC" block is replaced by a current control loop designed in the synchronous dq frame with the conventional decoupled control [19], [20]. The PI gains for the dq current controllers were designed for a 2 ms response time.

The linear controller is able to regulate the LC-StatCom and balance its capacitor voltages, despite the multiple saturations that take place during the transient. For example, the cluster voltage $v_{\Sigma-ab}$ becomes lower than its ac-side reference $|v_{ab}^\star|$ at $t = 0.027\,\text{s}$ for one tenth of the fundamental period approximately, as illustrated in Fig. 9(a). It can be seen that the corresponding modulation signal δ_{ab} is outside the range $[-1,\ 1]$ while $v_{\Sigma-ab} < |v_{ab}^\star|$, as shown in Fig. 9(f). The same phenomenon occurs in phase-arm bc, as can be seen in Figs. 9(b) and (f). Unlike the proposed constrained MPC, the conventional linear control lacks the ability to limit state variables, as it can be observed how the cluster voltage $v_{\Sigma-ca}$ exceeds its top limit, and accordingly so the five individual capacitor voltages embedded in phase-arm ca do, as illustrated in Figs. 9(c) and (e). As it can be seen in Fig. 9, the arm currents take approximately a complete cycle to settle to their reference values, while the proposed control offers transient responses of less than a quarter of the period. This delay of a period is caused by distorted capacitor voltages during this time.

For the sake of completeness, three different cases with an uncertainty in the capacitance parameter of a 10% has been carried out, i.e., a case where only one capacitor in phase-arm *ab* deviates 10% from its nominal value, a second case

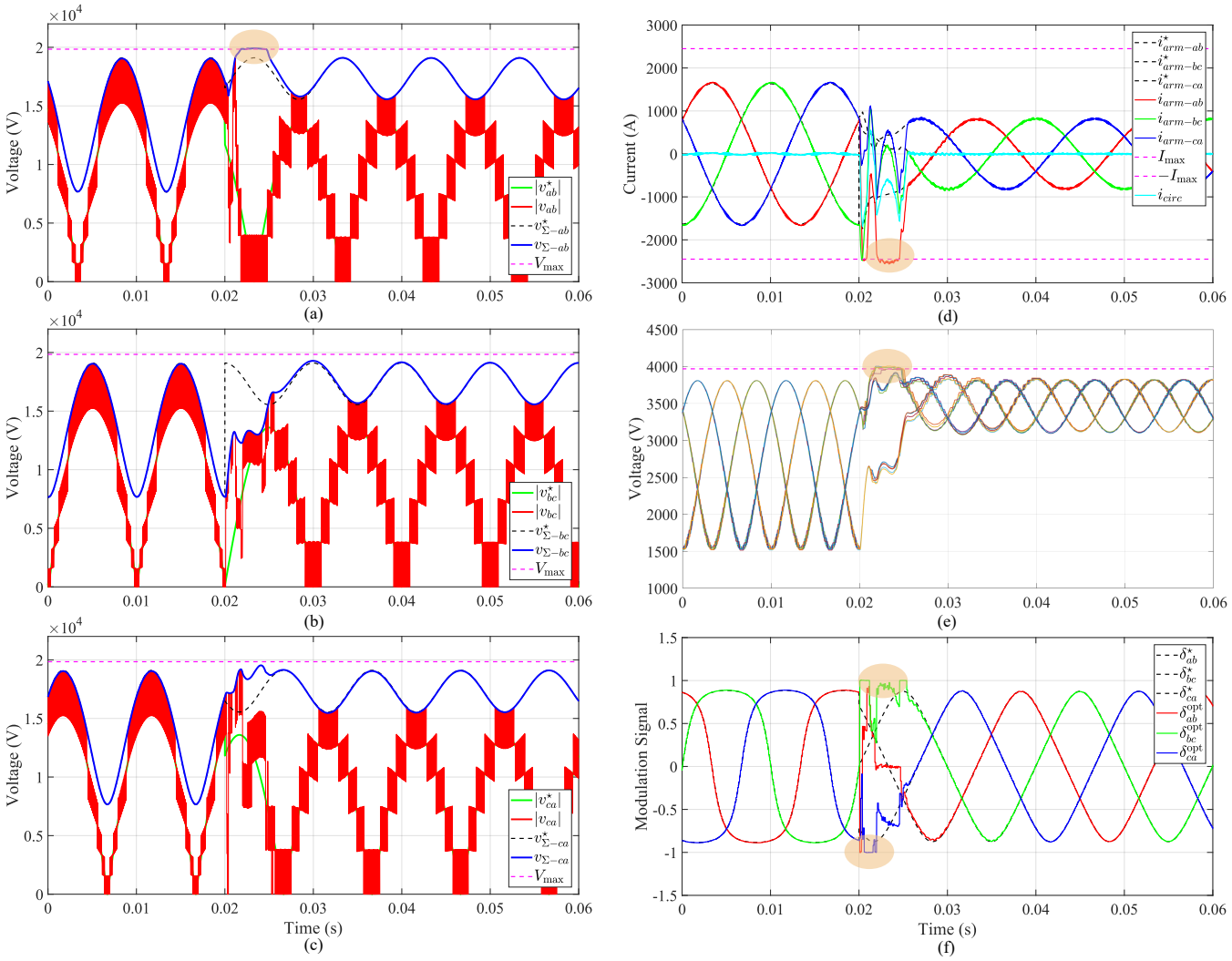

Fig. 8. LC-StatCom simulation waveforms, when using the proposed constrained MPC, during a sudden reactive power change from 100%-rated power capacitive-mode to 50%-rated power inductive-mode at $t = 0.02\,\text{s}$. (a) Phase-arm ab voltages v_{ab}, $v_{\Sigma-ab}$, (b) phase-arm bc voltages v_{bc}, $v_{\Sigma-bc}$, (c) phase-arm ca voltages v_{ca}, $v_{\Sigma-ca}$, (d) arm currents i_{arm-ab}, i_{arm-bc}, i_{arm-ca}, (e) the 15 individual capacitor voltages, and (f) optimal modulation signals δ_{ab}^{opt}, δ_{bc}^{opt}, δ_{ca}^{opt}.

where three capacitors in phase-arm *ab* deviate 10%, and a last case where all the capacitors in phase-arm *ab* deviate 10%. The worst-case scenario, which corresponds to the last case in 100%-rated power capacitive-mode, presents a maximum error in instantaneous capacitor voltage lower than 17.5%, 6% and 13%, in phase-arms *ab*, *bc* and *ca*, respectively, with respect to their nominal references, and a mean deviation lower than 5.3%, 2.3% and 4.8% along a fundamental period. Besides, there is not significative error in current waveforms. In addition, despite the parametric uncertainty, waveforms show a fast and stable transient, and that capacitor voltages are properly limited by the proposed constrained MPC.

VI. Conclusion

A constrained MPC approach for the control of three-phase multilevel LC-StatComs has been implemented, specifically for CHB converters with delta configuration. The proposed MPC approach considers the bilinear nature of the LC-StatComs. The paper shows how the accuracy of the model predictions improves by applying the proposed concept of inter-sampling. Furthermore, the proposed MPC approach considers the reference design and the adaptation of the outer control loop to LC-StatComs. Moreover, a comprehensive set of control design constraints adapted to the LC-StatCom has been proposed. The constrained MPC approach results in fast transient response and the ability to constrain the voltage value across the relatively small capacitors. The paper has presented a comprehensive set of experimental measures that corroborates computational feasibility. For the reported cases, the proposed predictions enhancement results in the elimination of steady-state oscillations in the circulating current of approximately 10%, and improvement in the THD of the grid currents from 1.46% to 0.30% (80% improvement). Also, simulation results show the improved performance of the proposed MPC compared with a more conventional control approach based on PI regulators in the *dq* frame. For the studied cases, the proposed

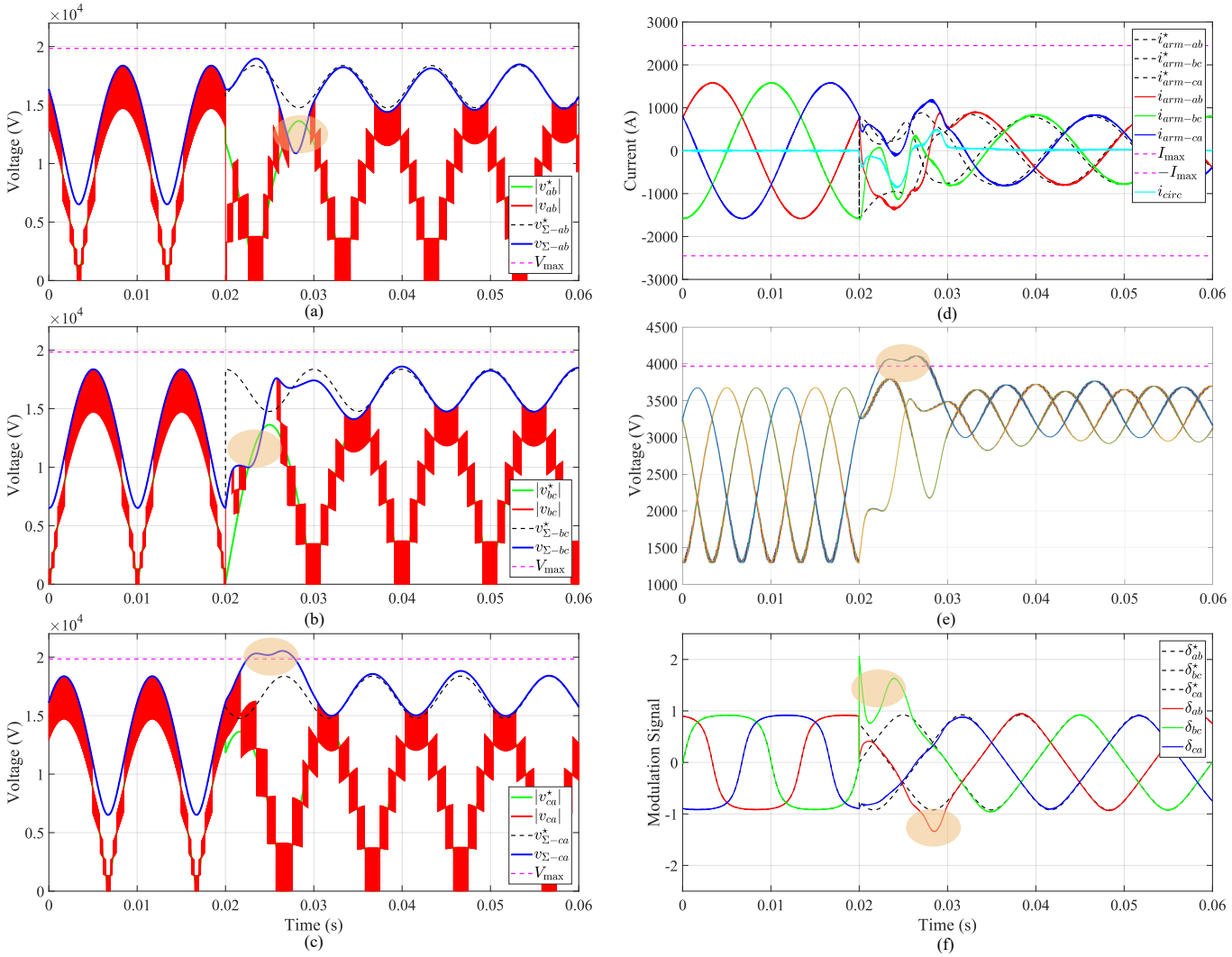

Fig. 9. LC-StatCom simulation waveforms, when using a current control designed in the synchronous dq frame with the conventional decoupled control, during a sudden reactive power change from 100%-rated power capacitive-mode to 50%-rated power inductive-mode at $t = 0.02$ s. (a) Phase-arm ab voltages v_{ab}, $v_{\Sigma-ab}$, (b) phase-arm bc voltages v_{bc}, $v_{\Sigma-bc}$, (c) phase-arm ca voltages v_{ca}, $v_{\Sigma-ca}$, (d) arm currents i_{arm-ab}, i_{arm-bc}, i_{arm-ca}, (e) the 15 individual capacitor voltages, and (f) modulation signals δ_{ab}, δ_{bc}, δ_{ca}.

approach is approximately four times faster in current transients, while it is able to limit the individual capacitor voltages. Therefore, the proposed MPC can be an effective solution to control LC-StatComs, providing good dynamic performance while effectively containing the capacitor voltages and arm currents within safe operating regions, as experimental and simulation results have corroborated.

APPENDIX

This Appendix provides the differential equations of the three independent currents of the bilinear CHB system model with continuous variables in (7), i.e., i_a, i_b, i_{circ}.

From the circuit shown in Fig. 1, the instantaneous three-phase PWM converter voltages v_{ab}, v_{bc}, v_{ca} can be obtained as,

$$\begin{bmatrix} v_{ab} \\ v_{bc} \\ v_{ca} \end{bmatrix} = L_{arm}\frac{d}{dt}\begin{bmatrix} i_{arm-ab} \\ i_{arm-bc} \\ i_{arm-ca} \end{bmatrix} + R_{arm}\begin{bmatrix} i_{arm-ab} \\ i_{arm-bc} \\ i_{arm-ca} \end{bmatrix} + \boldsymbol{E}_1\left(L\frac{d}{dt}\begin{bmatrix} i_a \\ i_b \\ i_c \end{bmatrix} + R\begin{bmatrix} i_a \\ i_b \\ i_c \end{bmatrix} + \begin{bmatrix} e_a \\ e_b \\ e_c \end{bmatrix}\right), \quad (81)$$

with

$$\boldsymbol{E}_1 = \begin{bmatrix} 1 & -1 & 0 \\ 0 & 1 & -1 \\ -1 & 0 & 1 \end{bmatrix}. \quad (82)$$

The injected StatCom currents i_a, i_b, i_c are linear combinations of the arm currents i_{arm-ab}, i_{arm-bc}, i_{arm-ca}; the phase a injected current, for example, is given by $i_a = i_{arm-ab} - i_{arm-ca}$. The injected currents for the phases b and c are defined accordingly. Further analysing the relationship

between the arm currents and the injected StatCom currents, and defining the circulating current as

$$i_{circ} = \frac{1}{3}\left(i_{arm-ab} + i_{arm-bc} + i_{arm-ca}\right), \tag{83}$$

the following relationship for the converter arm currents is obtained:

$$\begin{bmatrix} i_{arm-ab} \\ i_{arm-bc} \\ i_{arm-ca} \end{bmatrix} = \frac{1}{3}\boldsymbol{E}_1 \begin{bmatrix} i_a \\ i_b \\ i_c \end{bmatrix} + \boldsymbol{U}_3 i_{circ}, \tag{84}$$

with $\boldsymbol{U}_3 = [1\ 1\ 1]^T$.

Substituting (84) into (81), the instantaneous three-phase PWM converter voltages in the stationary *abc* frame can be expressed as follows:

$$\begin{bmatrix} v_{ab} \\ v_{bc} \\ v_{ca} \end{bmatrix} = \boldsymbol{E}_1 \left(L_{eq}\frac{d}{dt}\begin{bmatrix} i_a \\ i_b \\ i_c \end{bmatrix} + R_{eq}\begin{bmatrix} i_a \\ i_b \\ i_c \end{bmatrix} + \begin{bmatrix} e_a \\ e_b \\ e_c \end{bmatrix} \right) + \boldsymbol{U}_3 \left(L_{arm}\frac{di_{circ}}{dt} + R_{arm} i_{circ} \right), \tag{85}$$

where $R_{eq} = R + R_{arm}/3$ and $L_{eq} = L + L_{arm}/3$ represent the equivalent resistance and inductance, respectively. Equation (85) governs the currents dynamics.

REFERENCES

[1] G. Farivar, B. Hredzak, and V. G. Agelidis, "Reduced-capacitance thin-film H-bridge multilevel STATCOM control utilizing an analytic filtering scheme," *IEEE Trans. Ind. Electron.*, vol. 62, no. 10, pp. 6457–6468, Oct. 2015.

[2] G. Farivar, C. D. Townsend, B. Hredzak, J. Pou, and V. G. Agelidis, "Low-capacitance cascaded H-bridge multilevel StatCom," *IEEE Trans. Power Electron.*, vol. 32, no. 3, pp. 1744–1754, Mar. 2017.

[3] G. Farivar, C. D. Townsend, B. Hredzak, J. Pou, and V. G. Agelidis, "Passive reactor compensated cascaded H-bridge multilevel LC-StatCom," *IEEE Trans. Power Electron.*, vol. 32, no. 11, pp. 8338–8348, Nov. 2017.

[4] G. Farivar, C. Townsend, J. Pou, and B. Hredzak, "Low-capacitance StatCom with modular inductive filter," *IEEE Trans. Power Electron.*, vol. 34, no. 4, pp. 3192–3203, Apr. 2019.

[5] G. Farivar, C. Townsend, H. Dehghani Tafti, Y. Jeon, E. Rodriguez, J. Pou, and B. Hredzak, "Cascaded H-bridge low capacitance static compensator with modular switched capacitors," *IEEE Trans. Ind. Electron.*, pp. 1–1, 2020.

[6] Y. Jeon, C. D. Townsend, H. Dehghani Tafti, E. Rodriguez Ramos, G. G. Farivar, J. Park, and J. Pou, "An enhanced static compensator with DC-link voltage shaping method," *IEEE Trans. Power Electron.*, vol. 35, no. 3, pp. 2488–2500, 2020.

[7] E. R. Rodriguez, R. Leyva, Q. Liu, C. D. Townsend, G. G. Farivar, S. Ceballos, and J. Pou, "Enhancing inductive operation of low-capacitance cascaded H-bridge StatComs using optimal third-harmonic circulating current," *IEEE Trans. Power Electron.*, pp. 1–1, 2021.

[8] E. Rodriguez, G. G. Farivar, N. Beniwal, C. D. Townsend, H. D. Tafti, S. Vazquez, and J. Pou, "Closed-loop analytic filtering scheme of capacitor voltage ripple in multilevel cascaded H-bridge converters," *IEEE Trans. Power Electron.*, vol. 35, no. 8, pp. 8819–8832, Aug. 2020.

[9] T. Isobe, L. Zhang, H. Tadano, J. A. Suul, and M. Molinas, "Control of DC-capacitor peak voltage in reduced capacitance single-phase S-TATCOM," in *Proc. IEEE 17th Workshop on Control and Modeling for Power Electron. (COMPEL)*, pp. 1–8, Jun. 2016.

[10] Z. He, L. Zhang, T. Isobe, and H. Tadano, "Dynamic performance improvement of single-phase STATCOM with drastically reduced capacitance," in *Proc. IEEE 3rd Intern. Future Energy Electron. Conf. and ECCE Asia (IFEEC 2017 - ECCE Asia)*, pp. 1413–1418, Jun. 2017.

[11] E. R. Ramos, R. Leyva, G. G. Farivar, H. D. Tafti, C. D. Townsend, and J. Pou, "Incremental passivity control in multilevel cascaded H-bridge converters," *IEEE Trans. Power Electron.*, vol. 35, no. 8, pp. 8766–8778, Aug. 2020.

[12] X. Ge and F. Gao, "Flexible third harmonic voltage control of low capacitance cascaded H-bridge STATCOM," *IEEE Trans. Power Electron.*, vol. 33, no. 3, pp. 1884–1889, Mar. 2018.

[13] D. Niu, T. Hao, F. Gao, T. Xu, X. Meng, F. Qin, Z. Ma, and X. Ge, "Cascaded packed U-cell STATCOM with low capacitance and its third harmonic control," in *Proc. IEEE Applied Power Electronics Conference and Exposition (APEC)*, pp. 529–534, Jun. 2020.

[14] G. Farivar, B. Hredzak, and V. G. Agelidis, "Decoupled control system for cascaded H-bridge multilevel converter based STATCOM," *IEEE Trans. Ind. Electron.*, vol. 63, no. 1, pp. 322–331, Jan. 2016.

[15] M. Hagiwara, R. Maeda, and H. Akagi, "Negative-sequence reactive-power control by a PWM STATCOM based on a modular multilevel cascade converter (MMCC-SDBC)," *IEEE Trans. Ind. Appl.*, vol. 48, no. 2, pp. 720–729, Mar. 2012.

[16] J. I. Leon, S. Vazquez, and L. G. Franquelo, "Multilevel converters: Control and modulation techniques for their operation and industrial applications," *Proc. of the IEEE*, vol. 105, no. 11, pp. 2066–2081, Nov. 2017.

[17] H. Akagi, S. Inoue, and T. Yoshii, "Control and performance of a transformerless cascade PWM STATCOM with star configuration," *IEEE Trans. Ind. Appl.*, vol. 43, pp. 1041–1049, Jul. 2007.

[18] J. I. Y. Ota, Y. Shibano, and H. Akagi, "A phase-shifted PWM D-STATCOM using a modular multilevel cascade converter (SSBC)-part II: Zero-voltage-ride-through capability," *IEEE Trans. Ind. Appl.*, vol. 51, pp. 289–296, Jan. 2015.

[19] H. Sugimoto, S. Morimoto, and M. Yano, "A high performance control method of a voltage-type PWM converter," in *Proc. IEEE Power Electronics Specialists Conference (PESC)*, pp. 360–368 vol.1, Apr. 1988.

[20] S. Saadate, P. Nonnon, R. L. Doeuff, and D. Escallier, "PWM force-commutated GTO converter in four quadrant operation," in *Proc. IEEE Industrial Electronics Conference (IECON)*, pp. 600–605 vol.1, Oct. 1991.

[21] J. Maciejowski, *Predictive Control: With Constraints*. Prentice Hall, 2002.

[22] T. Geyer, *Model predictive control of high power converters and industrial drives*. John Wiley & Sons, 2016.

[23] Y. Zhang, X. Wu, and X. Yuan, "A simplified branch and bound approach for model predictive control of multilevel cascaded H-bridge STATCOM," *IEEE Trans. Ind. Electron.*, vol. 64, no. 10, pp. 7634–7644, Oct. 2017.

[24] C. D. Townsend, T. J. Summers, J. Vodden, A. J. Watson, R. E. Betz, and J. C. Clare, "Optimization of switching losses and capacitor voltage ripple using model predictive control of a cascaded H-bridge multilevel StatCom," *IEEE Trans. Power Electron.*, vol. 28, no. 7, pp. 3077–3087, Jul. 2013.

[25] V. Spudic and T. Geyer, "Model predictive control based on optimized pulse patterns for modular multilevel converter STATCOM," *IEEE Trans. Ind. Appl.*, vol. 55, no. 6, pp. 6137–6149, Nov. 2019.

[26] M. Chai, N. B. Y. Gorla, and S. K. Panda, "Fault detection and localization for cascaded H-bridge multilevel converter with model predictive control," *IEEE Trans. Power Electron.*, vol. 35, no. 10, pp. 10109–10120, Oct. 2020.

[27] E. Rodriguez, G. G. Farivar, J. Pou, H. D. Tafti, C. D. Townsend, and S. Vazquez, "A generalized voltage balancing algorithm for modular multilevel cascaded converters," in *Proc. ECCE*, pp. 214–218, Sep. 2019.

[28] W. Brogan, *Modern Control Theory*. Prentice Hall, 1991.

[29] B. O'Donoghue, G. Stathopoulos, and S. Boyd, "A splitting method for optimal control," *IEEE Trans. Control Systems Technology*, vol. 21, no. 6, pp. 2432–2442, 2013.

[30] J. Pou, S. Ceballos, G. Konstantinou, V. G. Agelidis, R. Picas, and J. Zaragoza, "Circulating current injection methods based on instantaneous information for the modular multilevel converter," *IEEE Trans. Ind. Electron.*, vol. 62, no. 2, pp. 777–788, Feb. 2015.

[31] M. Odavic, V. Biagini, P. Zanchetta, M. Sumner, and M. Degano, "One-sample-period-ahead predictive current control for high-performance active shunt power filters," *IET Power Electronics*, vol. 4, no. 4, pp. 414–423, Apr. 2011.

[32] P. Cortes, J. Rodriguez, P. Antoniewicz, and M. Kazmierkowski, "Direct power control of an AFE using predictive control," *IEEE Trans. Power Electron.*, vol. 23, no. 5, pp. 2516–2523, Sep. 2008.

[33] Y. Zhang, W. Xie, Z. Li, and Y. Zhang, "Model predictive direct power control of a PWM rectifier with duty cycle optimization," *IEEE Trans. Power Electron.*, vol. 28, no. 11, pp. 5343–5351, Nov. 2013.

[34] J. Rawlings and D. Mayne, *Model predictive control: Theory and design*. Nob Hill Pub., 2009.

[35] B. Kouvaritakis and M. Cannon, *Model Predictive Control: Classical, Robust and Stochastic*. Advanced Textbooks in Control and Signal Processing, Springer, London, 2015.

[36] G. Farivar, H. Dehghani Tafti, C. D. Townsend, E. Rodriguez, and J. Pou, "Load adaptive cascaded H-bridge low capacitance StatCom with modular capacitors," in *Proc. IECON*, vol. 1, pp. 3541–3546, 2019.

[37] B. Stellato, G. Banjac, P. Goulart, A. Bemporad, and S. Boyd, "OSQP: An operator splitting solver for quadratic programs," *ArXiv e-prints*, Nov. 2017.

[38] G. Banjac, P. Goulart, B. Stellato, and S. Boyd, "Infeasibility detection in the alternating direction method of multipliers for convex optimization," *Journal of Optimization Theory and Applications*, vol. 183, no. 2, pp. 490–519, 2019.